Published in final edited form as:
Cell Rep. 2022 September 13; 40(11): 111329. doi:10.1016/j.celrep.2022.111329.

Histone H1 regulates non-coding RNA turnover on chromatin in a m6A-dependent manner

José Miguel Fernández-Justel[1], **Cristina Santa-María**[1], **Sara Martín-Vírgala**[1], **Shreya Ramesh**[1], **Alberto Ferrera-Lagoa**[1], **Mónica Salinas-Pena**[2], **Javier Isoler-Alcaraz**[1], **Magdalena M. Maslon**[3,4,5], **Albert Jordan**[2], **Javier F. Cáceres**[3], **María Gómez**[1,6,*]

[1]Centro de Biología Molecular Severo Ochoa (CBMSO), Consejo Superior de Investigaciones Científicas/Universidad Autónoma de Madrid (CSIC/UAM), Nicolás Cabrera 1, 28049 Madrid, Spain

[2]Instituto de Biología Molecular de Barcelona (IBMB-CSIC), Carrer de Baldiri Reixac, 15, 08028 Barcelona, Spain

[3]MRC Human Genetics Unit, Institute of Genetics and Cancer, University of Edinburgh, Crewe South Road, Edinburgh EH4 2XU, UK

Summary

Linker histones are highly abundant chromatin-associated proteins with well-established structural roles in chromatin and as general transcriptional repressors. In addition, it has been long proposed that histone H1 exerts context-specific effects on gene expression. Here, we identify a function of histone H1 in chromatin structure and transcription using a range of genomic approaches. In the absence of histone H1, there is an increase in the transcription of non-coding RNAs, together with reduced levels of m6A modification leading to their accumulation on chromatin and causing replication-transcription conflicts. This strongly suggests that histone H1 prevents non-coding RNA transcription and regulates non-coding transcript turnover on chromatin. Accordingly, altering the m6A RNA methylation pathway rescues the replicative phenotype of H1 loss. This work unveils unexpected regulatory roles of histone H1 on non-coding RNA turnover and m6A deposition, highlighting the intimate relationship between chromatin conformation, RNA metabolism, and DNA replication to maintain genome performance.

*Correspondence: mgomez@cbm.csic.es.
[4]Present address: Center for Advanced Technology, Adam Mickiewicz University, Uniwersytetu Poznanskiego 10, 61-614 Poznań, Poland
[5]Present address: Department of Gene Expression, Institute of Molecular Biology and Biotechnology, Adam Mickiewicz University, Uniwersytetu Poznanskiego 6, Poznań, Poland
[6]Lead contact

Author Contributions

J.M.F.-J., C.S.-M., S.M.-V., S.R., A.F.-L., M.S.-P., and J.I.-A. performed experiments. J.M.F.-J. performed all computational analyses. J.M.F.-J., C.S.-M., and M.G. designed and analyzed the experiments. M.M.M. contributed to the TT-seq experimental design and analysis. M.G. conceived the project, analyzed experiments, and wrote the article. M.G., A.J., and J.F.C. secured the funding. All authors analyzed the data, discussed the results, and approved the final version of the manuscript.

Declaration of Interests

The authors declare no competing interests.

Europe PMC Funders Author Manuscripts

Europe PMC Funders Author Manuscripts

Abstract

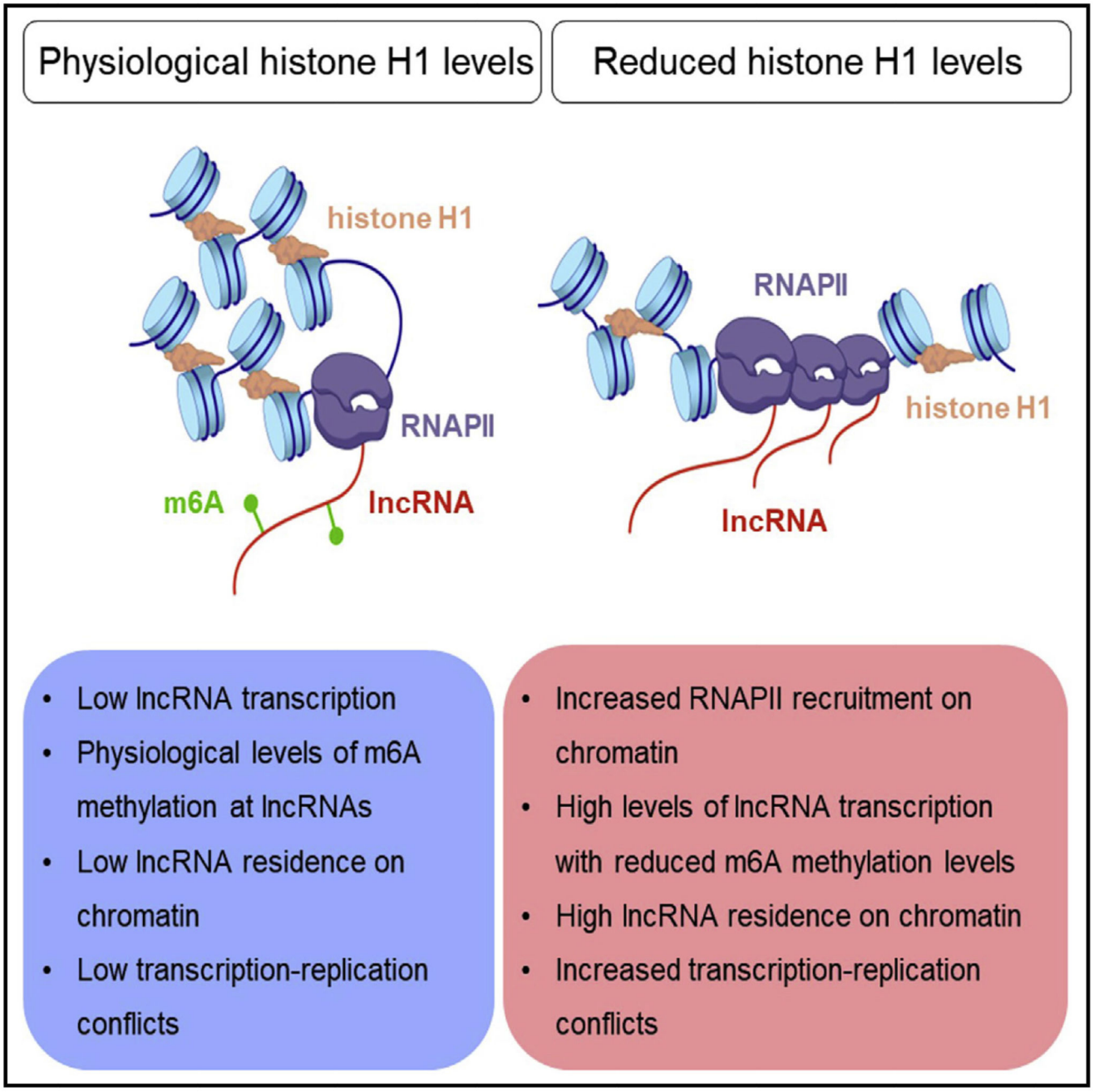

Graphical abstract.

Introduction

Linker histone H1 plays an essential role in the folding of nucleosome arrays into more compact chromatin structures. Importantly, growing evidence from the past decade supports

the concept that histone H1 is a multifunctional protein that can block the binding of other proteins to chromatin and also act as a recruitment platform for activators or repressors thus fine-tuning chromatin function (Hergeth and Schneider, 2015; Fyodorov et al., 2018). There are seven genes coding for somatic linker histone H1 subtypes or variants in the mouse and human genomes, with an average of 0.5 to 1.3 H1 molecule per nucleosome depending on cell type (Woodcock et al., 2006). Disruption of one or two linker histone genes, initially performed to delineate subtype-specific functions, revealed that cells can maintain their total H1 content through compensatory upregulation of the remaining H1 genes (Fan et al., 2001). However, inactivation of three subtypes leading to a 50% of the normal level of H1 resulted in embryonic lethality in mice, demonstrating that a correct stoichiometry of linker histone deposition on chromatin is essential for mammalian development (Fan et al., 2005). Embryonic stemcells (mESCs) derived from these triple-knockout embryos (H1-TKO) have a genomic average of one H1 molecule every four nucleosomes. These cells display limited changes in gene expression, yet they display de-repression of major satellite elements (Fan et al., 2005; Cao et al., 2013; Geeven et al., 2015).

The distribution of histone H1 throughout the genome is not uniform. It has been shown that chromatin at active and poised gene promoters is characterized by reduced histone H1 levels, while inactive genes and heterochromatin are enriched in H1 (Izzo et al., 2013; Cao et al., 2013; Millán-Ariño et al., 2014). In addition, H1 mediates the silencing of heterochromatic repetitive elements by both modulating their higher order structure and interacting with the histone methyltransferases responsible for the repressive methylation of these regions (Healton et al., 2020). The dual role of H1 is not limited to heterochromatin, as it also affects chromatin architecture by interacting directly with both transcriptional activators and/or repressors. Some examples include H1 binding to Cul4A ubiquitin ligase and the PAF1 elongation complexes that help maintain active gene expression (Kim et al., 2013a, 2013b), its recruitment by the Msx1 factor to a regulatory element in the MyoD gene resulting in repressed muscle cell differentiation (Lee et al., 2004), or its interaction with p53 repressing its transcriptional activation effect (Kim et al., 2008).

We previously found that reductions on histone H1 content generated genome-wide alterations in their replication initiation patterns, as well as massive fork stalling and DNA damage due to replication-transcription conflicts (Almeida et al., 2018). These findings raised the question of how limited alterations in gene expression upon H1 deficiency can be reconciled with wide-spread replication-transcription conflicts. To delineate additional functions of histone H1 on transcription regulation, in this study we performed a detailed analysis of chromatin transcript abundances, RNA polymerase II (RNAPII) location and activity, and nascent RNA N-6-adenosine methylation (m6A) profiling in H1-TKO-deficient mESCs (triple knockout for the subtypes *H1c*, *H1d*, and *H1e)*. We found that reductions in histone H1 content resulted in the presence of thousands of *cis*-regulatory non-coding transcripts bound to chromatin. These non-coding RNAs (ncRNAs) were actively transcribed upon H1 deficiency, anchored to chromatin through RNAPII complexes, and also displayed reduced levels of m6A. Remarkably, knockdown of the m6A demethylases ALKBH5 and FTO, and the m6A reader YTHDC1, rescues the replicative stress of H1-TKO cells. These results indicate that an appropriate histone H1 content is required to limit ncRNA accumulation on chromatin, likely by both reducing RNAPII recruitment, leading to

a decrease in their transcription, and facilitating co-transcriptional m6A deposition, which affects their stability. Our findings reveal an unexpected role of histone H1 in regulating non-coding RNA turnover in chromatin and uncover a link between chromatin conformation and RNA post-transcriptional modifications, with important implications for understanding genome functionality.

Results

Reductions in histone H1 content lead to the accumulation of non-coding transcripts on chromatin

A variety of models of H1 depletion in different systems showed limited transcriptional alterations, comprising both up- and down-regulation of specific sets of genes (Shen and Gorovsky, 1996; Hashimoto et al., 2010; Vujatovic et al., 2012; Fan et al., 2005; Sancho et al., 2008; Geeven et al., 2015; Izquierdo-Boulstridge et al., 2017). To investigate the mechanism by which H1 deficiency leads to transcription-dependent replicative stress we searched for chromatin-enriched RNAs in H1-TKO mESCs, using the chromatin-enriched RNA sequencing (CheRNA-seq) approach (Werner and Ruthenburg, 2015). This technique preferentially detects RNAs bound to chromatin through RNA polymerase molecules, thus enabling the analysis of partially processed transcripts, as well as of structural RNAs (Figure 1A). The enrichment of chromatin-associated transcripts in CheRNA preparations was monitored by checking the chromatin/nucleoplasm ratio for *Kcnq1ot1* and *Neatl*, two non-coding RNAs that associate to chromatin post-transcriptionally, relative to *Klf16* and *Nat8L*, two normally exported mRNAs (Werner and Ruthenburg, 2015) (Figure 1B). Inclusion of a spike-in luciferase RNA allowed to assess potential changes in the overall amount of chromatin-bound RNA between preparations (Figure S1A). Normalized reads from triplicate experiments from wild-type (WT) or H1-TKO mESCs were used to build a *de novo* transcriptome, and transcripts were classified in four classes regarding their genome location and coding potential: (1) internal antisense RNAs (IAS), (2) long intergenic non-coding RNAs (lncRNAs), (3) promoter upstream transcripts (PROMPTs), and (4) coding RNAs (coding) (Figure S1B). CheRNA-seq analyses revealed thousands of differentially expressed transcripts comprising the four categories (fold change > 2 and adjusted $p < 0.01$) (Figure 1C). Strikingly, all non-coding classes were upregulated in H1-TKO cells (Figures 1D and 1E; blue, upregulated in WT, and red, upregulated in TKO). In addition, intergenic reads not statistically included in the *de novo* transcriptome were also higher in H1-TKO cells (Figures S1C and S1D). These findings indicate that an appropriate histone H1 content is required to prevent the accumulation of non-coding transcripts in chromatin.

Accumulated non-coding transcripts are regulatory RNAs

Functional analysis of gene expression revealed the enrichment of gene categories related to cell differentiation and development among differentially abundant coding transcripts (Figure S2A). Consistently, the promoters of differential coding transcripts were overrepresented in Polycomb features, like SUZ12 binding sites and H3K27 trimethylation (Figures S2B and S2C), and mapped to Polycomb chromatin states as defined in Juan et al. (2016) (Figure S2D). In agreement, upregulated genes in histone H1-depleted cells were very lowly expressed in WT conditions, and the histone mark composition of their promoter

regions was not significantly changed relative to downregulated ones (Figures S2E and S2F). These findings agreed with earlier work linking histone H1 with Polycomb complexes (Kim et al., 2015), a connection that was not detected in mRNA preparations (Geeven et al., 2015) likely due to the strong enrichment for low-expressed and unstable RNAs in the CheRNA samples.

Chromatin-associated non-coding RNAs frequently have *cis*-regulatory functions (Werner et al., 2017; Gil and Ulitsky, 2020). To evaluate whether the lncRNAs unveiled in mESCs upon a reduction in histone H1 levels were indeed enhancing the activity of neighboring promoters, we first calculated the expression levels of coding genes relative to their distance to a differentially expressed lncRNA (Werner and Ruthenburg, 2015; Werner et al., 2017) (Figure 2A). This analysis showed that the closer to a lncRNA, the higher the transcriptional activity of a gene. Consistent with this, a large fraction of upregulated non-coding transcripts were generated from enhancer-like chromatin regions (Figure 2B), and displayed enrichment in H3K4me1 around their transcription start sites (TSSs) (Figure 2C). Likewise, lncRNAs with differential enrichment in H1-TKO cells were preferentially located in *cis* of genes functionally involved in development and RNAPII transcription (Figure 2D). A deeper analysis of this last group revealed that it comprised key transcription factors involved in cell differentiation, including the pluripotency factors *Nanog*, *Sox2*, *Pou5f* (*Oct3/4)*, and *c-Myc*. In all cases, the lncRNAs TSSs mapped at the superenhancer (SE) regions that regulate the transcription of these genes in embryonic stem cells (Li et al., 2014; Blinka et al., 2016; Liao et al., 2013) (Figure 2E). We subsequently examined the dbSUPER database and found that, out of the 231 annotated SE in mESCs (Khan and Zhang, 2016), 227 matched an assembled lncRNA. Thus, the chromatin-associated lncRNAs unmasked when histone H1 levels are reduced fulfill the requirements of regulatory RNAs. As the functional terms of the differential lncRNA-neighbor genes were similar to the set of differentially expressed coding genes (Figure S2A), we checked whether the accumulation of non-coding transcripts in H1-TKO chromatin was altering the expression of the proximal coding gene. We found that the fold change between lncRNA expression and that of its neighbor coding gene was correlated for downregulated, but not for upregulated lncRNAs (Figures 2F and S2G). In the examples shown in Figure 2E, *Nanog*, *Sox2*, and *Pouf5* SE-derived lncRNAs are upregulated in H1-TKO cells, while their corresponding mRNAs are unchanged. On the contrary, *Myc* gene, as well as its SE-derived lncRNA are downregulated in H1-TKO cells. A similar trend was detected for IAS and PROMPTs, despite their lower numbers (Figures S2H and S2I). Collectively, these data suggest that histone H1 is a repressor of (silent) regulatory lncRNAs which, in its absence, accumulate in chromatin likely contributing to the replicative phenotype.

Depleting histone H1 levels in human cells triggers non-coding transcript accumulation in chromatin and transcription-dependent replicative stress

To confirm that the accumulation of non-coding transcripts in chromatin was consequence of histone H1 depletion, rather than an indirect effect related to the lack of differentiation potential of H1-TKO mESCs (Zhang et al., 2012), we next analyzed the transcriptional status of human differentiated cells knocked down for histone H1 (Izquierdo-Boulstridge et al., 2017). We applied the same computational pipeline designed for CheRNA-seq data to

re-analyze published total RNA sequencing (RNA-seq) data from breast cancer T47D cells upon doxycycline-induced knockdown for the subtypes H1.2 and H1.4 (shMultiH1, human homologues of the murine *H1c* and *H1e*, respectively) (Figure S3A; Izquierdo-Boulstridge et al., 2017). Despite the reduced representation of non-coding transcripts in total RNA preparations relative to chromatin-RNA preparations, lncRNA transcription was enhanced upon induction of histone H1 silencing (Figure 3A). We confirmed that lncRNAs were enriched in CheRNA preparations relative to nucleoplasm (Figure 3B, brown bars), and that their genomic loci were marked by H3H4me1 (Figure S3B, left panel). In addition, the chromatin accumulation of differential lncRNAs increased upon histone H1 depletion (Figure 3B, light brown bars), as well as the local levels of H3H4me3 (Figure S3B).

We then asked whether this short-term histone H1 depletion also recapitulate the replicative stress we described for H1-TKO mESCs (Almeida et al., 2018). DNA fiber analysis showed significant decreases in fork rate and increases in fork asymmetry upon H1 reduction (Figures 3C–3E, light brown bars). Most importantly, the replicative phenotypes were transcription dependent, as both were readily reverted when inhibiting RNAPII elongation activity by 5,6-dichlorobenzimidazole1-β-D-ribofuranoside (DRB) treatment. The elevated DNA damage signaling of these cells was concomitantly reduced by transcription inhibition (Izquierdo-Boulstridge et al., 2017; Figure S3C). Altogether, these results indicate that reducing histone H1 content in human differentiated cells increases transcription-dependent replicative stress that might be mediated by enhanced non-coding RNA chromatin association.

Accumulated transcripts are tethered to chromatin by RNAPII and can form R-loops

To address how ncRNAs are transcribed upon H1 deficiency, we next investigated RNAPII genomic occupancies. We performed chromatin immunoprecipitation sequencing (ChIP-seq) using human chromatin as a spike-in control to detect quantitative differences in chromatin-bound RNAPII between cell types (see STAR Methods) and found a 12% increase in RNAPII in H1-TKO chromatin (Figure S4A; quality controls for RNAPII ChIP-seq data are shown in Figures S4B–S4D). However limited, this excess in RNAPII complexes was not uniformly distributed through the genome but specifically located around the TSS of accumulated transcripts in H1-TKO chromatin (Figures S4E and S4F). Changes in the levels of coding transcripts, lncRNAs and IAS were accompanied by parallel changes in the levels of RNAPII at their TSS in either cell type (Figure 4A). Moreover, promoter-proximal regions of lncRNAs and IAS upregulated in H1-TKO cells recruited almost as much RNAPII as some coding promoters (Figure 4A, lower panels). To ensure that differential transcripts anchored to chromatin by RNAPII complexes were actively transcribed, we conducted nascent transcriptome sequencing assays (TT-seq; Schwalb et al., 2016). We found a positive correlation between RNA synthesis rates and chromatin transcript abundances for all RNA classes, indicating that the residence time of nascent transcripts on chromatin is related to their production (Figures 4B and 4C). In agreement with this, changes in nascent expression between cell types correlated with RNAPII gains in H1-TKO cells, both for coding and lncRNAs (Figure S4G). To further investigate the transcription dynamics of CheRNAs, we next compared the RNAPII pausing index of the various transcript classes. We found that lncRNAs in general displayed lower

pausing indexes than coding RNAs and that upregulated coding RNAs have decreased RNAPII pausing (Figure 4D). Interestingly, RNAPII pausing at upregulated lncRNAs was significantly higher in H1-TKO cells than in WT cells (Figure 4D, insets). These analyses support the idea that reductions in histone H1 levels in chromatin results in increased recruitment of RNAPII molecules engaged in active transcription, a fraction of which can be paused at TSS of lncRNAs, altogether potentially impeding the advance of moving replication forks.

Transcripts that remain longer in the transcription bubble can give rise to RNA:RNA hybrid structures (R-loops), a potential source of replication-transcription conflicts in mammalian cells (reviewed by García-Muse and Aguilera, 2019). We have previously shown that R-loops accumulate in H1-TKO cells and that transient overexpression of RNAseH partially restored the slow fork progression phenotype (Almeida et al., 2018). To investigate R-loop formation at CheRNA loci, we performed MapR, a technique that takes advantage of a catalytic deficient mutant of RNaseH fused to micrococcal nuclease to release and sequence DNA regions containing R-loop structures (Figures S5A and S5B) (Yan et al., 2019). As previously reported, MapR preferentially detects R-loop enrichments at TSS of active genes (Figure S5C) (Yan et al., 2019). Accordingly, R-loop levels paralleled CheRNA levels at all transcript categories (Figures 4E and S5D), confirming that R-loop formation is increased in histone H1-depleted chromatin likely contributing to the replicative phenotype.

Chromatin-associated transcripts have reduced levels of m6A modification

Chromatin-associated regulatory RNAs, including PROMPTs and enhancer RNAs, are marked by m6A modification, which destabilizes their levels in chromatin (Liu et al., 2020). Thus, to identify specific features of lncRNA transcripts repressed by H1, we first focused on m6A. This modification is co-transcriptionally deposited on RNAPII transcripts by the METTL3/METTL14 writer complex and read by YTH domain-containing proteins (Zaccara et al., 2019). Intriguingly, several members of the writer complex accessory proteins, as well as the m6A nuclear reader YTHDC1, have been identified as high-confidence interactors of multiple histone H1 subtypes in human cells by proteomics approaches (Zhang et al., 2016). We hypothesized that non-coding transcripts in H1-TKO cells might accumulate in chromatin due not only to an increased transcription (Figure 4) but also to alterations in m6A modification. In agreement with this idea, global m6A levels were decreased on CheRNA preparations in H1-TKO cells relative to their WT counterparts (Figure 5A). To confirm these findings and to determine m6A changes at specific transcript classes we coupled CheRNA purification with m6A immunoprecipitation and sequencing (ChMeRIP-seq), using an *in vitro* methylated RNA as spike-in control (see STAR Methods). ChMeRIP reads distribution across gene bodies recapitulated the TSS- and stop codon-proximal accumulation reported by m6A immuno-precipitation and sequencing (MeRIP-seq) from total RNA in mESCs (Liu et al., 2020, 2021; Xu et al., 2021) (Figures S6A and S6B). It also detects m6A enrichments at characterized lncRNAs, as exemplified by *Malat1* or *Neat1* loci (Patil et al., 2016; Liu et al., 2021) (Figure S6C). As anticipated from the global m6A CheRNA measurements, ChMeRIP-seq analyses revealed significantly reduced levels of methylation in H1-TKO cells for both coding and non-coding transcripts (Figures 5B and S6A). Of note, lncRNAs displayed higher m6A levels than coding RNAs in WT

mESCs chromatin (Figure 5B), a finding that is suggestive of distinct post-transcriptional regulation dynamics for non-coding transcripts. Interestingly, m6Alosses in H1-TKO cells were significantly higher at lncRNAs, specifically at the upregulated lncRNA category (Figure 5C; representative examples in Figure 5D), which consistently harbors higher binding densities of the m6A catalytic subunit METTL3 at their promoter regions in WT mESCs (Figure S6D; data from Xu et al., 2021). m6A deposition was not qualitatively different between cell types, as exemplified by the ChMeRIP profiles at the previously defined m6A peaks of the genes *Ythdc1* or *Spen* (Figure S6B) or at the lncRNAs *Malat1* or *Neatl* (Figure S6C) (Wei et al., 2021). None of these transcripts were differentially abundant on H1-TKO chromatin, and quantitative assessment of m6A abundances at these defined peaks showed either a gain or no change in histone H1-depleted cells (intriguingly, themRNAencoding for the transcriptional repressor SPEN was markedly less methylated in H1-deficient cells) (Figure 5E). In contrast, all upregulated lncRNAs tested displayed reductions in m6A levels to various extents in H1-TKO cells, indicating that m6A losses are a hallmark of chromatin accumulated lncRNAs. To characterize the transcripts mostly affected by m6A loss, we sorted them by nascent RNA abundances and histone H1 promoter-proximal occupancies in WT cells. We found that maximal reductions inm6A levels correlated with lower transcript expression and higher histone H1 occupancy in WT cells (Figures 5F and 5G). As noted before, these associations were stronger for non-coding transcripts (Figures 5F and 5G, lower panels), albeit also occur at coding RNAs (Figures 5F and 5G, upper panels). Altogether, these results provide evidence supporting a connection between histone H1 and m6A levels of chromatin-associated lncRNAs.

To sustain these findings further, we next examined m6A and chromatin RNA abundances of H1-TKO differentially expressed RNAs in mESCs depleted of METTL3 (*Mettl3*-KO) (Liu et al., 2020). As expected, m6A levels were reduced in *Mettl3*-KO cells, irrespectively of the transcript category analyzed (Figure S6E, empty bars). Notably, we identified a positive correlation between expression alterations in both mutant scenarios: up or downregulated lncRNAs in H1-TKO cells were also up- or down-regulated in *Mettl3*-KO cells (Figure S6F, empty bars). These observations suggest that, while affecting similarly all types of transcripts, reduced m6A levels specifically stabilize non-coding transcripts that are retained in chromatin in histone H1-depleted cells. Similar analyses in cells depleted of the m6A nuclear reader YTHDC1 revealed that RNA abundances were negatively correlated in all cases between histone H1- or METTL3-depleted and YTHDC1-depleted cells (Figure S6F, gray bars), suggesting that YTHDC1 is implicated in the differential stability of these non-coding transcripts.

Reduced methylation of lncRNAs alters their chromatin turnover, triggering replication-transcription conflicts

Taken together, these analyses indicate that reductions in histone H1 levels results in the altered turnover of non-coding transcripts in chromatin in a m6A-dependent manner. This interpretation makes the prediction that increasing m6A levels in H1-TKO cells will destabilize non-coding transcripts in chromatin, thus alleviating the replicative stress phenotype (Figure 6A). To test this prediction we first used reversible short interfering RNA (siRNA) to deplete the m6A erasers, ALKBH5 and FTO (Figure 6B, first and second

panels). Then, we analyzed replication dynamics by fiber stretching. Interestingly, the depletion of either demethylase restored the replication fork speed of H1-TKO cells toward WT levels (Figure 6C, first and second panels). Analogous effects were observed by a combined depletion of both demethylases (Figures S7A and S7B), or by exposing the cells to the alpha-ketoglutarate dependent demethylases inhibitor R-2-hydroxyglutarate (R2-HG) in conditions in which overall DNA synthesis was not detectably altered (Figures S7C and S7D). To ensure that CheRNA upregulation was still occurring upon ALKBH5/FTO inhibition we quantified the chromatin/nucleoplasm ratio of several lncRNAs in H1-TKO cells after R2-HG treatment (Figure S7E). Notably, the reversal of the replicative phenotype occurs despite of high levels of lncRNAs on chromatin, suggesting that the relative decrease in m6A modification is the main contributor of the replicative impairment of these cells. This interpretation was confirmed by knocking down the m6A writer METTL3, resulting in slow elongating forks in WT mESCs, without further aggravating the H1-TKO replicative phenotype (Figures 6B and 6C, third panels). Thus, METTL3 seems to function in the same pathway as histone H1 to regulate m6A levels on chromatin-associated lncRNAs. Intriguingly, replication fork speeds in H1-TKO were also fully restored upon knockdown of the m6A reader YTHDC1 (Figure 6C, fourth panel), even though its expression was only decreased by 30% in H1-TKO cells (Figure 6B, fourth panel). Altogether, these results imply a requirement for appropriate m6A levels and a role of YTHDC1 on chromatin-bound lncRNAs to allow smooth replication fork progression.

Finally, to evaluate the function of m6A modification on lncRNAs in genome performance, we investigated replication-transcription conflicts by proximity ligation assay (PLA) between the elongating form of RNAPII phosphorylated at Ser2 (RNAPIIS2P) and PCNA, a key component of the replisome. Nuclear PLA foci were clearly higher in H1-TKO cells, strengthening the conclusion that the replicative stress of histone H1-depleted cells was due to replication-transcription clashes (Figures 6D and S7F). In concordance with the recovery of fork velocities, FTO or YTHDC1 depletion, but not METTL3 depletion, significantly decreased PLA foci in H1-TKO cells (Figure 6E). We conclude that histone H1 and m6A installation at lncRNAs prevent replication-transcription conflicts.

Discussion

In all organisms studied, reductions in H1 levels do not cause global upregulation of transcription but rather affect a reduced set of genes (Shen and Gorovsky, 1996; Hellauer et al., 2001; Fan et al., 2005; Sancho et al., 2008; Hashimoto et al., 2010; Vujatovic et al., 2012; Geeven et al., 2015). By examining nascent transcription and RNAPII occupancies in WT and H1-TKO mES cells we expanded these findings to around 1,300 upregulated and 1,600 downregulated genes, mostly implicated in cell differentiation and development. Altered H1 content likely affects RNAPII recruitment at those TSS sites directly, as the chromatin architecture of the promoter-proximal region of differentially expressed genes was not significantly changed. We further show that H1 depletion allowed increased recruitment of RNAPII complexes driving transcription of thousands of non-coding RNAs derived by superenhancers of neighboring coding genes, 75% of which were not previously annotated in the mouse genome (ENSEMBL non-coding transcriptome). Strikingly, we found that lncRNAs harbor reduced levels of m6A modification, causing their stabilization

on chromatin and thus generating conflicts with advancing replication forks (Figure 7). We conclude that histone H1 has a fundamental role in controlling the potential toxic effects of excessive levels of chromatin-associated ncRNAs. These findings are relevant as they uncover a link between an essential component of chromatin and the m6A non-coding regulatory axis, with important implications for genome integrity.

Although m6A modification is best studied for coding RNAs, m6A profiling studies (Patil et al., 2016) have shown that it is also present in lncRNAs (Meyer et al., 2012). Methylation of *XIST* lncRNA contributes to its transcriptional repression effects through the recruitment of the nuclear m6A binding protein YTHDC1 (Patil et al., 2016), although the extent of its contribution to *XIST*-mediated chromosomal silencing remains controversial (Nesterova et al., 2019). The question of how m6A modification is selectively directed to specific RNAs is not yet clear. It has been proposed that the RNA-binding proteins RBM15 and RBM15B, that associate with the WTAP-METTL3/14 complex, enable the binding of the m6A writer complex to multiple RNAs, including *XIST* (Patil et al., 2016). In a similar fashion, the components of the WTAP complex VIRMA (virilizer homolog), WTAP (Wilms tumor associated protein), ZC3H13, and CBLL1/Hakai, all of which interact with histone H1 (Zhang et al., 2016), are putative candidates to mediate substrate RNA specificity. Because reductions in m6A levels correlate positively with histone H1 occupancy in WT cells, we speculate that the presence of H1 at lncRNAs loci will abrogate RNAPII recruitment at their TSS sites, and also facilitate co-transcriptional m6A deposition, thus ensuring appropriate non-coding transcript turnover. Indeed, m6A-RNA turnover dynamics is executed by reader proteins, and several mechanisms have been proposed depending on the type of RNA and the cellular context (Roundtree et al., 2017; Ries et al., 2019). Conditional knockout of YTHDC1 in mESCs enhances the stability of repeat RNAs transcribed by transposons (Liu et al., 2020), and initiates cellular reprogramming to a 2C-like state (Liu et al., 2021). On the other hand, YTHDC1-m6A RNAs can form phase-separated nuclear condensates that maintain mRNA stability suppressing myeloid leukemic differentiation (Cheng et al., 2021). The intriguing finding that YTHDC1 depletion in H1-TKO cells rescues the replicative phenotype similarly to ALKBH5/FTO depletion suggests that YTHDC1 is required for the stability of lncRNAs even when m6A levels are impaired. This is in agreement with a recent preprint showing that YTHDC1 mediates the chromatin association and gene expression effects of HOTAIR lncRNA regardless of the ablation of its major m6A site (Porman et al., 2020). The authors propose that differential affinities of YTHDC1 for distinct m6A sites might mediate the functionally diverse and context dependent effects observed even for a single lncRNA. Further experiments are required to determine both the mechanisms of H1-mediated m6A deposition and m6A-mediated fate at individual lncRNAs.

Our work highlights yet another example of the multi-faceted functions of histone H1 beyond chromatin architecture. We propose that histone H1 functions as a regulator of lncRNA metabolism. These findings add onto the hypothesis that the multi-functionality of linker histones can be explained through H1-protein interactions that directly regulate recruitment of proteins to chromatin (Hergeth and Schneider, 2015; Kalashnikova et al., 2016). The adaptability of the intrinsically disordered N- and C-terminal domains of H1 likely facilitates the wide range of specific protein-protein interactions reported (Kalashnikova et al., 2013; Szerlong et al., 2015; Zhang et al., 2016). Accordingly, the

disordered terminal domains acquire secondary structure when bound to DNA (Roque et al., 2005), nucleosomes (Lu and Hansen, 2004; Fang et al., 2012), and possibly other proteins. Recent studies addressing histone H1 distribution in the three-dimensional nucleus showed that, in differentiated cells, local H1 density regulates the degree of chromatin compaction through maintaining a condensed and spatially distinct chromatin B compartment (Serna-Pujol et al., 2020; Willcockson et al., 2021). In line with this, decompaction of three-dimensional chromatin has been proposed as the dominant effect of H1 loss of function occurring in B cell lymphomas (Yusufova et al., 2021). Given the implication of histone H1 in lncRNA modification and chromatin retention unveiled here, it is tempting to speculate that some of the defects associated with diseases carrying histone H1 missense mutations, such as certain cancers or Rahman syndrome (Landau et al., 2015; Reddy et al., 2017; Ciolfi et al., 2020), could be mediated by lncRNAs altering the maintenance of proper chromatin compartmentalization, or nuclear bodies formation (Saitoh et al., 2004; Xiao et al., 2016).

In conclusion, our work emphasizes the crucial role of histone H1 as a transcriptional regulator, whose full characterization awaits multiple studies in the coming years. As anticipated by A. P. Wolffe, “understanding the molecular mechanisms by which histone H1 exerts its functions might uncover new ways to manipulate gene expression” (Wolffe, 1997).

Limitations of the study

Even though our work shows that histone H1 and METTL3 function on the same pathway to regulate m6A levels on nascent ncRNAs, we cannot exclude the possibility that the increased rates of transcription occurring in the absence of H1 might also contribute to less efficient co-transcriptional m6A deposition. The molecular details linking histone H1, m6A writers, down-stream effectors of m6A modification and ncRNA removal from chromatin remain to be elucidated. We propose that YTHDC1 protects ncRNAs from degradation, regardless of their m6A levels, through a process that might involve nuclear bodies formation and surely requires further investigation.

Because the stability of R-loop structures is regulated by the m6A modification of the RNA component (Abakir et al., 2020), we cannot discard that the reduced levels of m6A in H1-depleted cells will also increase R-loops levels on chromatin, contributing to the elevated rates of replication-transcription conflicts observed in these cells.

Star★Methods

Key Resources Table

REAGENT or RESOURCE	SOURCE	IDENTIFIER
Antibodies		
Rat monoclonal anti-CIdU	Abcam	Catab6326; RRID:AB_305426
Mouse monoclonal IgG1 anti-IdU	BD Biosciences	347580; RRID:AB_10015219
Mouse monoclonal IgG2a anti-ssDNA	Millipore	MAB3034; RRID:AB_94645
Anti-rat IgG Alexa-Fluor 594	ThermoFisher	A-11007; RRID:AB_10561522

REAGENT or RESOURCE	SOURCE	IDENTIFIER
Anti-mouse IgG1 Alexa-Fluor 488	ThermoFisher	A-21121; RRID:AB_2535764
Anti-mouse IgG2a Alexa-Fluor 647	ThermoFisher	A-21241; RRID:AB_2535810
Mouse monoclonal anti-γH2AX (Ser139)	Millipore	05-636; RRID:AB_309864
Anti-mouse Alexa-Fluor 488	ThermoFisher	A-21202; RRID:AB_141607
Mouse monoclonal anti-RNAPII	Millipore	05-623; RRID:AB_309852
Rabbit polyclonal anti-m6A	Synaptic Systems	202003; RRID:AB_2279214
Anti-H3K4me3	Abcam	ab8580; RRID:AB_306649
Anti-H3K4me1	Abcam	ab8895; RRID:AB_306847
Rabbit IgG	Millipore	12-370; RRID:AB_145841
Mouse monoclonal IgG2a anti-PCNA (PC10)	Santa Cruz	sc-56; RRID:AB_628110
Rabbit polyclonal anti-phospho RNAPII (Ser2)	Bethyl lab	A300-654A; RRID:AB_519341
Chemicals, peptides, and recombinant proteins		
Mouse LIF	Millipore	ESG1106
DRB (5,6-Dichlorobenzimidazole 1-β-Dribofuranoside)	Sigma	D1916
R-2-HG (R-2-hydroxyglutarate)	Sigma	H8378
Lipofectamine 2000 Reagent	ThermoFisher	11668027
IdU (5-Iodo-2'-deoxyuridine)	Sigma	I7125
CldU (5-Chloro-2'-deoxyuridine)	Sigma	C6891
TRIzol Reagent	ThermoFisher	15596026
HotStarTaq DNA polymerase	Qiagen	203205
4sU (4-thiouridine)	Sigma	T4509
EZ-Link HPDP-Biotin	Pierce	21341
RiboLock RNase Inhibitor (40 U/μL)	ThermoFisher	EO0381
BioMag®Plus Concavalin A	Polysciences	86057-3
Critical commercial assays		
Ribo-Zero rRNA Removal Kit	Illumina	20040526
TruSeq Stranded Total RNA Library Prep	Illumina	20020596
RNeasy MinElute Cleanup column	Qiagen	74204
QiAquick Gel extraction Kit	Qiagen	28704
NEBNext DNA Library Prep Kit	New England Biolabs	E6040
NEBNext Ultra II DNA Library Prep Kit	New England Biolabs	E7645
NEBNext Ultra Directional RNA Library Prep Kit	New England Biolabs	E4720
Mouse RiboPOOL kit	siTOOLs Biotech GmbH	K006-000055
Duolink®In Situ Red Starter Kit Mouse/ Rabbit	Merck	DUO92101
Deposited data		
CheR-seq	This paper	GEO: GSE166426
RNAPII ChIP-seq	This paper	GEO: GSE166426
TT-seq	This paper	GEO: GSE166426
ChMeRIP-seq	This paper	GEO: GSE166426

REAGENT or RESOURCE	SOURCE	IDENTIFIER
MapR	This paper	GEO: GSE166426
H3K4me1, H3K4me3 and H3K27me3 ChIP-seq	Geeven et al., (2015)	GEO: GSE75426
shMulti RNAseq	Izquierdo-Boulstridge et al. (2017)	GEO: GSE83277
Mettl3-WT, Mettl3-KO and Ythdc1-KO meRIP-seq	Liu et al. (2020)	GEO: GSE133600
Mettl3 ChIP-seq	Xu et al. (2021)	GEO: GSE126243
H1c and H1d ChIP-seq	Cao et al. (2013)	GEO: GSE46134
Experimental models: Cell lines		
H1-TKO mES cells	Fan et al. (2001)	N/A
shMulti T47D cells	Izquierdo-Boulstridge et al. (2017)	N/A
Oligonucleotides		
Primers for quantitative real-time PCR, see Table S1	This paper	N/A
Primers for ChIP-qPCR, see Table S2	This paper	N/A
siRNA targeting sequences, see Table S3	This paper	N/A
Recombinant DNA		
GST-MNase	Addgene	Plasmid#136291
GST-RHΔ-MNase	Addgene	Plasmid#136292
Software and algorithms		
Tophat2	Kim et al. (2013a), 2013b	https://ccb.jhu.edu/software/tophat/index.s/html
Samtools	Li et al., 2009	http://samtools.sourceforge.net/
Cufflinks	Trapnell et al. (2010)	http://cole-trapnell-lab.github.io/cufflinks/
Salmon	Patro et al. (2017)	https://combine-lab.github.io/salmon/
DESeq2	Love et al. (2014)	https://bioconductor.org/packages/release/bioc/html/DESeq2.html
Panther	Mi et al. (2019)	http://pantherdb.org/
Enrichr	Kuleshov et al. (2016)	https://maayanlab.cloud/Enrichr/
BWA mem	N/A	http://bio-bwa.sourceforge.net/bwa.shtml
Bowtie	Langmead et al. (2009)	http://bowtie-bio.sourceforge.net/index.shtml
MACS2	Zhang et al. (2008)	https://github.com/macs3-project/MACS
R 3.6.0	N/A	https://www.r-project.org/
Other		
SDS2.4	Applied Biosystems	N/A
Prism v7	GraphPad	N/A

Resource Availability

Lead contact—Further information and requests for resources and reagents should be directed to and will be fulfilled by the lead contact, María Gómez (mgomez@cbm.csic.es).

Materials availability—This study did not generate new reagents.

Experimental Model And Subject Details

Cell lines—Mouse embryonic stem cells WT and H1-TKO were kindly provided by Arthur Skoultchi and authenticated by assessing histone *H1c*, *H1d* and *H1e* depletion on NGS experiments. Human breast cancer T47D cells inducible knock-down for the subtypes H1.2 and H1.4 upon doxycycline treatment were previously described in Izquierdo-Boulstridge et al. (2017) and authenticated by RT-qPCR.

Method Details

Cell culture, siRNA transfection, and drug treatments—Mouse embryonic stem cells were grown in DMEM (Invitrogen) supplemented with 10% fetal bovine serum (Biosera), 1 × non-essential aminoacids (Gibco), 1mM sodium piruvate (Gibco), 2mM L-glutamine (Gibco), 50 μM β-mercaptoethanol (Gibco), 10^3 U/mL LIF (ESGRO), 100 U/mL penicillin (Invitrogen) and 100 μg/mL streptomycin (Invitrogen), at 37°C and 5% CO_2. For transcription inhibition experiments, cells at 80% confluency were treated with 100 μM 5,6- dichlorobenzimidazole 1-b-d-ribofuranoside (DRB) (Sigma) for 3 hours. For small interfering RNAs (siRNA) transfection, Lipofectamine™ 2000 (Thermo) was used to deliver siRNAs into mES cells. 40nM of each siRNA was diluted in 1mL of OPTIMEM and incubated for at least 20 min with Lipofectamine diluted in OPTIMEM. Cells were tripsinized, resuspended in medium without antibiotics and added to the previous mix of Lipofectamine and siRNA. After incubating cells for 15 min at RT, cells were seeded into new plates. Transfected cells were analyzed after 24h. All siRNAs were purchased from Sigma. For FTO/ALKBH5 inhibition, cells were treated with 20 or 40 mM R-2-hydroxyglutarate (R2-HG) (Sigma) for 24h. T47D inducible H1 knock-down cells were grown in RPMI 1640 medium, supplemented with 10% FBS, 2mML-glutamine, 100 U/mL penicillin, and 100 mg/mL streptomycin at 37°C with 5% CO2. Depletions were induced by 3 days exposure to 2.5 μg/mL doxycycline (Sigma) as described (Izquierdo-Boludstridge et al., 2017). All cells tested negative for mycoplasm infection.

Flow cytometry—For cell-cycle analyses, cells were pulse-labeled for 20 min with 250 μM IdU (Sigma) and fixed overnight in 70% ethanol at -20°C. Cells were then incubated in 2 M HCl (Merck) with 0.5% Triton X-100 (Sigma) for 30 min and neutralized with 0.1 M Sodium Tetraborate pH 9.5 (Merck) for 2 min before blocking 10 min with a solution of 1% BSA (Sigma) and 0.5% Tween20 (Sigma) in PBS. Afterwards cells were incubated for 1 hour with mouse anti-BrdU antibodies (BD Biosciences) followed by 30 minutes incubation with antimouse IgG Alexa-Fluor 647 antibodies (Thermo Fisher Scientific) at RT. Cells were finally stained with 2μg/ml DAPI (Merck) for another 10 minutes in the dark at RT. All samples were processed in a FACSCanto II (Becton Dickinson) with FACSDiva v6.1.3 software and analysed with the FlowJo v10 program.

Chromatin enriched RNA (CheRNA) sequencing—CheRNA preparations were obtained as described in Werner and Ruthenburg (2015). Briefly, 40 × 10^6 mES cells were lysed in 800 μL ice-cold Lysis Buffer A (10 mM Tris pH 7.5, 0.1% NP-40, 150 mM NaCl) for 5 min on ice. Nuclei were collected by sucrose cushion centrifugation (24% sucrose

in lysis buffer A), rinsed with ice-cold PBS + 1mM EDTA, and resuspended in 500μL ice-cold Glycerol Buffer (20 mM Tris pH 7.9, 75 mM NaCl, 0.5 mM EDTA, 0.85 mM DTT, 0.125 mM PMSF, 50% glycerol). Nuclei were lysed by adding one volume of ice-cold Lysis Buffer B (10mMHEPES pH 7.6, 1mM DTT, 7.5 mM $MgCl_2$, 0.2 mM EDTA, 0.3M NaCl, 1M urea, 1% NP-40) and kept on ice for 10 min, with periodic vigorous shaking. Insoluble chromatin was sedimented by centrifugation at 14000g and 4°C for 2 min, rinsed twice with cold PBS + 1mM EDTA, and resuspended in 100 μL PBS. At this point, 10 pg of an *in vitro* transcribed luciferase RNA was added to both the nucleoplasmic and chromatin samples as a spike-in control. RNAs were purified using TRIzol™, following manufacturer's instructions. Before library preparation, ribosomal RNA was depleted from the samples by a treatment with Ribo-Zero rRNA Removal Kit (Illumina). Libraries were generated using TruSeq Stranded Total RNA Library Prep (Illumina), and sequenced by 1 × 75 single reads at the Fundacion Parque Científico de Madrid.

DNA fiber stretching—Exponentially growing cells were pulsed consecutively for 20 min with 50 mM CldU (Sigma) and 250 mM IdU (Sigma). Collected cells were resuspended in cold PBS at a concentration of 0.5×10^6 cells/mL, and 2μL of this cell suspension was lysed through the addition of 10 μL of spreading buffer (200 mM Tris pH 7.4,50 mM EDTA, 0.5% SDS) on the top of a microscopy slide at 30°C. After 6 min of incubation in a humidity chamber at RT, DNA fibers were stretched by leaning the slide with a 30° slope. Slides were air dried and fixed at -20°C with 3:1 methanol:acetic acid solution, incubated with 2.5M HCl solution for 30 min at RT, washed three times with PBS, and treated with blocking solution (1% BSA, 1% Triton X-100 in PBS) for 1 h. Samples were sequentially incubated with primary antibodies; 1:100 anti-CldU (Abcam), 1:100 anti-IdU (Bencton Dickinson) and 1:3000 anti-ssDNA (Millipore) for one hour, and with secondary antibodies; 1:300 anti-rat IgG Alexa-Fluor 594, anti-mouse IgG1 Alexa-Fluor 488 and anti-mouse IgG2a Alexa-Fluor 647 (Invitrogen) for 30 min. Slides were mounted with Prolong Diamond (Invitrogen) and fibers visual acquisition was performed with an Axiovert200 Fluorescence Resonance Energy Transfer microscope (Zeiss) using the 40 × oil objective. Images were analyzed with ImageJ software, considering a conversion factor of 1 μm = 2.59 kb (Jackson and Pombo, 1998). Fork rates were calculated by measuring the length (kb) of the IdU track divided by the duration of the pulse (min), and fork asymmetries were obtained by calculating the percentage of the difference between the lengths of both CldU and IdU tracks of each replication fork. Statistical analysis of all data was performed with Prism v7 (GraphPad Software) using the non-parametric Mann-Whitney rank sum test.

Immunofluorescence—Cells grown on glass coverslips (VWR) were fixed with 3.7% formaldehyde in PBS for 15 min at RT and permeabilized with 0.5% Triton X-100 in PBS for 20 min at RT. Samples were blocked with 3% BSA (Sigma) in PBS before overnight incubation at 4°C with antibodies anti-γH2AX (1:250) (Millipore), followed by 1 h incubation at RT with antibodies anti-rabbit Alexa-Fluor 488 (Invitrogen) and 5 min staining at RT with 2ng/μL of DAPI (Merck) in PBS. Coverslips were mounted in Prolong Diamond (Life Technologies) and visual acquisition was performed in a A1R + confocal microscope (Nikon) using a either a 40× or a 60× oil objective. Nuclear segmentation

was based on DAPI staining. Statistical analyses were performed in Prism v7 (GraphPad Software) using the non-parametric Mann-Whitney rank sum test.

Chromatin immunoprecipitation and quantitative real time PCR (ChIP-qPCR)—Chromatin immunoprecipitation was performed according to the Upstate (Millipore) standard protocol. Briefly, cells were fixed using 1% formaldehyde for 10 min at 37°C, chromatin was extracted and sonicated to generate fragments between 200 and 500 bp. Next, 30 μg of sheared chromatin was immunoprecipitated overnight with the indicated antibody. Immunocomplexes were recovered using 20 μL of protein A magnetic beads, washed and eluted. Cross-linking was reversed at 65°C overnight and immunoprecipitated DNA was recovered using the IPure Kit (Diagenode). Genomic regions of interest were identified by real-time PCR (qPCR) using SYBR Green Master Mix (Invitrogen) and specific oligonucleotides in a QuantStudio™ 5 Real-Time PCR System machine (ThermoFisher Scientific). Each value was corrected by the corresponding input chromatin sample.

Retrotranscription and quantitative real-time PCR—SuperscriptIII was used to generate the cDNA following manufacturer's instructions. qPCR reactions were performed in an ABI Prism 7900HT Detection System (Applied Biosystems), using HotStarTaq DNA polymerase (Qiagen) following manufacturer's instructions. For absolute quantification, the Ct of each amplicon was interpolated in a standard curve obtained from the amplification of genomic DNA at five different concentrations (from 0.2ng/μL to 125ng/μL) and analyses were carried out with the SDS2.4 software (Applied Biosystems).

RNAPII chromatin immunoprecipitation sequencing (ChIP-seq)—Crosslinkings were performed in culture medium with 1% formaldehyde during 15 min at RT. After stopping the reactions with 125 mM glycine for 5 min, cells were washed twice with PBS and collected by scrapping in ice-cold PBS supplemented with protease and phosphatase inhibitors (10 μM leupeptin, 100 μM PMSF, 1μM pepstatin, 2 μg/mLaprotinin, 5 mM NaF, 1mM $NaVO_3$). Cells were centrifuged at 200g for 5 min, resuspended in cold Lysis Buffer (50 mM Tris pH 8, 1% SDS, 10 mM EDTA, protease and phosphatase inhibitors) at a concentration of 2×10^7 cells/mL and incubated on ice for 20 min. Soluble chromatin was fragmented on a Covaris sonication system by 40 cycles at 20% intensity, during 20 min 100 μg of the fragmented chromatin was diluted 1:10 in Dilution Buffer (20 mM Tris pH 8, 1% Triton X-100, 2mM EDTA, 150mM NaCl, protease and phosphatase inhibitors), and 5 μg of human chromatin, obtained from a MCF10A cell line following the same protocol, was added as spike-in control. Precleared chromatin was incubated overnight with 25 μg of anti-RNApoIII antibody (Millipore) at 4°C with gentle agitation, followed by a 2 h incubation with 200 μL of A/G protein beads. Immunocomplexes were washed sequentially with four different buffers, all supplemented with protease and phosphatase inhibitors: low salt buffer (10 mM Tris pH 8, 0.1% SDS, 1% Triton X-100, 2mM EDTA, 150 mM NaCl), high salt buffer (20 mM Tris pH 8, 0.1% SDS, 1% Triton X-100, 2mM EDTA, 500 mM NaCl), LiCl buffer (10 mM Tris pH 8, 0.25M LiCl, 1% NP40, 1% Na-deoxycholate, 1mM EDTA) and TE buffer (10 mM Tris pH 8, 1mM EDTA). Finally, chromatin was eluted with elution buffer (0.1M $NaHCO_3$, 1% SDS), crosslinkings were reverted, and DNA was purified with phenol-chloroform extraction and ethanol precipitation. Libraries

were generated with the NEBNext Ultra II DNA Library Prep Kit (New England Biolabs) following the manufacturer's recommendations and sequenced by 1 × 75 single-reads at Fundación Parque Científico de Madrid.

Transient transcription sequencing (TTseq)—Nascent transcription labeling assays were carried out as previously described (Schwalb et al., 2016; Maslon et al., 2019). 4-thiouridine (4sU) was added to sub-confluent cell cultures at a final concentration of 1 mM for 10 min before cell harvest. Cells were lysed directly on a plate with 5 mL of TRIzol (Invitrogen), total RNA was isolated following manufacturer's protocol and sonicated by two pulses of 30 s in a Bioruptor instrument. A total of 100 μg of sonicated RNA per cell line was used for biotinylation and purification of 4sU-labeled nascent RNAs. Biotinylation reactions consisted of total RNA and EZ-Link HPDP-Biotin dissolved in dimethylformamide (DMF) and were performed in labeling buffer (10 mM Tris pH 7.4, 1 mM EDTA) for 2 h with rotation at RT. Unbound Biotin-HPDP was removed by chloroform/isoamylalcohol (24:1) extraction in MaXtract tubes (Qiagen). RNA was precipitated with 10^{th} volume of 5M NaCl and 1 volume of isopropanol. Following one wash in 80% ethanol, the RNA pellet was left to dry and resuspended in 100 μL RNase-free water. Biotinylated RNA was purified using μMacs Streptavidin kit, eluted twice using 100 mM DTT and recovered using RNeasy MinElute Cleanup column (Qiagen) according to instructions. cDNA libraries were prepared using NEBNext Ultra Directional RNA Library Prep Kit (New England Biolabs) according to the manufacturer's instructions. Libraries were pooled and sequenced by 2 × 75 single-reads at Fundación Parque Científico de Madrid. Reads were aligned to the mm10 reference genome using Tophat2 (Kim et al., 2013a, 2013b) with standard parameters. bedGraph files loaded in the IGV browser were generated with the Bedtool genomecov.

CheRNA m6A-RNA immunoprecipitation (meRIP-seq)—CheRNAs were purified as described above, and 1 pg of *in vitro* transcribed N6-methylated Luciferase RNA per million cells was added as spike-in control before Trizol extraction. RNA fragmentation and meRIP were performed as described in Dominissini et al. (2013) and Zeng et al. (2018), with the following modifications. Aliquots containing 2 μg of CheRNAs in 18μL of DEPC H2O were fragmented by incubation with 2 μL of 100 uL Tris pH 7, 100 uL$ZnCl_2$ 1M, 800 uL DEPC water, at 70°C for 8 min, and reactions were stopped by adding 2 μL of 0.5M EDTA. A total of 50 μg of pooled fragmented CheRNAs were incubated with 5 μg of anti-m6A antibodies (Synaptic Systems) previously bound to A/G protein agarose beads (SantaCruz) in IP buffer (10 mM Tris-HCl pH 7.4, 150 mM NaCl, 0.1% Igepal CA-630), and supplemented with RiboLock™ (Thermo Scientific), during 6 h at 4°C. Beads were washed three times with IP buffer, meRNAswere eluted in elution buffer (10 mM Tris-HCl pH 7.4, 150 mM NaCl, 0.1% Igepal CA-630, 6.67mM m6A) and purified through RNeasy columns (Qiagen) following the manufacturers protocol. For qPCR analyses, (target-meRIP/spike-meRIP)/(target-input/spike-input), were represented per each region. Libraries for massive sequencing were generated using TruSeq Stranded Total RNA Library Prep (Illumina), without previous rRNA depletion, and sequenced by 1 × 75 single reads at the Centre for Genomic Regulation.

MapR—GST-MNase and GST-RHΔMNase protein expression and purification were carried out as described in Yan et al. (2019). MapR experiments were performed exactly as described in Yan et al. (2019) by exposing 5 millions of cells immobilized on Concavalin A-coated beads to 1μM of purified GST-MNase or GST-RHΔMNase proteins. MNase-released DNA fragments ranging between 200-1000 bp were size-purified from agarose gels using QIAquick gel extraction kit (Qiagen). Libraries were generated with the NEBNext Ultra II DNA Library Prep Kit (New England Biolabs) following the manufacturer's recommendations and sequenced by 2 × 50 pair-end reads on a NovaSeq platform at Fundación Parque Científico de Madrid.

m6A quantification by dot-blot—rRNA depletions were carried out at Fundación Parque Científico de Madrid. Briefly, 5 ug of CheRNAs were used as input at each depletion using RiboPOOL™ kit (siTOOLs Biotech GmbH) following manufacturer recommendations. Clean-up of rRNA-depleted RNAs were performed with Agencourt RNAClean XP (Beckman Coulter) and the resulting preparations were validated and quantified by 4200 TAPEStation (Agilent Technologies). 5 μg of CheRNA or 300 ng of rRNA-depleted CheRNA for each condition were denatured at 95°C for 5 min and transferred to a Hybond-XL membrane (Amersham) in a Bio-Dot® Microfiltration Apparatus (Bio-Rad) following manufacturer's instructions. Spotted RNAs were UV-crosslinked to the membrane in a Stratalinker® 1800 (Stratagene) at 120 mJoule/cm2. The signal detection was performed after hybridation with anti-m6A antibody (Synaptic Systems), using standard ECL detection reagents.

Proximity ligation assays—PLA was performed using Duolink PLA Technology (Merck), following the manufacturer's instructions. mESCs were permeabilized with 1% Triton X-100 + 4% paraformaldehyde in 1xPBS for 15 min at RT, washed with PBS, and fixed with 100% ice-cold Methanol for 15 min at 4°C before incubating with Duolink Blocking Solution for 1h at 37°C in a heated humidity chamber. Mouse anti-PCNA and rabbit anti-RNAPIIS2P antibodies were diluted 1:2000 in Duolink Antibody Diluent and incubated overnight at 4°C. Then, secondary antibody binding, ligation and amplification reactions were performed according to the manufacturer's guidelines. Duolink *in situ* PLA probe anti-rabbit PLUS, Duolink *in situ* PLA probe anti-mouse MINUS and Duolink Detection Reagents Red were used to perform the PLA reactions. Slides were mounted in Duolink *in situ* Mounting Medium with DAPI and visual acquisition was performed in a A1R + confocal microscope (Nikon) using a 60 × oil objective. DAPI-based nuclear segmentation and foci quantification were performed using FIJI homemade generated macros, available on request. PLA foci number per cell were quantified for all conditions (>300 cells/replicate). Statistical analyses were performed in Prism v7 (GraphPad Software) using the non-parametric Mann-Whitney rank sum test.

CheRNA-seq analysis—Reads were aligned to the mm10 reference genome and to the Luciferase coding sequence using Tophat2 (Kim et al., 2013a, 2013b) with standard parameters. bedGraph files loaded in the IGV browser were generated with the Bedtool genomecov. The scores of these files were normalized with the total number of aligned reads for each experiment. For the transcriptome assembly, reads coming from six experiments

(three WT and three H1-TKO replicates) were pulled, and separated in two files depending on the template strand (Watson or Crick), discriminating them with Samtool view -F 0 × 10 or -f 0 × 10, respectively. Spliced reads were discarded from the pull, by removing the entries with a CIGAR string which contained any 'N' character. The remaining reads were used to assemble a "genome-guided" transcriptome with Cufflinks v2.2.1 (Trapnell et al., 2010). This transcriptome was further curated with home-made scripts to remove low abundance transcripts (minimum coverage <2.5), remove very short transcripts (size <300 bp), merge proximal transcripts in the same strand (distance <2.5 kb) and split transcripts which included an already annotated TSS in the RefGene database. These transcripts were classified in four groups: coding, PROMPTs, lncRNAs and internal antisense transcripts (IASs), according to the diagram shown in Figure S1. After transcriptome assembly, 21702 coding transcripts, 3139 PROMPTs, 12673 lncRNAs and 2904 IASs were detected. For the differential gene expression analysis, the quantification of reads per transcript was performed with Salmon (Patro et al., 2017) using standard parameters. To select differentially expressed genes, DESeq2 software (Love et al., 2014) was used, setting two different thresholds: adjusted p-value < 0.01 and fold-change > 2. GO-term enrichment analyses were performed using Panther v14.1 software (Mi et al., 2019). To account for transcription factor and epigenetic enrichments, Enrichr software was employed (Kuleshov et al., 2016).

Histone H1 knock-down RNA-seq analysis—Reads from total RNA-seq preparations (Izquierdo-Boulstridge et al., 2017) were aligned to the hg19 reference genome using Tophat 2 with standard parameters. For the transcriptome assembly, reads coming from the six experiments (two controls, two H1.4-KD and two multi-KD) were pulled, and separated in two files depending on the template strand (Watson or Crick), discriminating them with Samtool view -F 0 × 10 or -f 0 × 10, respectively. The reads that matched a RefGene annotated coding gene were removed from the pull, and the remaining reads were used to assemble a "genome-guided" transcriptome with Cufflinks v2.2.1, exclusively from the non-coding part of the genome. This transcriptome was further curated with home-made scripts to remove low abundance transcripts (minimum coverage <2.5), remove very short transcripts (size <300 bp), merge proximal transcripts in the same strand (distance <2.5 kb) and split transcripts which included an already annotated TSS in the RefGene database. Finally, it was merged with the ENSEMBL coding transcriptome using Cuffmerge, and the transcripts were classified in the four same types as before: in the end, 22827 coding transcripts, 2420 PROMPTs, 14843 lncRNAs and 4562 IASs were detected. The differential gene expression analysis was performed as described above. In this case, the statistical thresholds were set as adjusted p-value <0.1 and fold-change > 2.

RNAP II ChIP-seq analysis—Reads were aligned to mouse mm10 and human hg19 reference genomes using bwa mem algorithm. In addition to the standard total read number normalization, the ratio between mouse and human reads was used to correct the H1-TKO cells metaplot signal, according to this formula:

$$TKOs = \frac{TKOr * mouseWTreads/humanWTreads}{mouseTKOreads/humanTKOreads}$$

where

TKO_s is the spike-in normalized RNApolII signal.

TKO_r is the total reads normalized RNApolII signal.

MapR analysis—Reads were aligned to the mm10 reference genome using bwa mem algorithm. The peak-calling was performed with MACS2 with standard parameters, without the use of a genomic input.

ChMeRIP-seq analysis—Reads were aligned to the mm10 reference genome using Tophat2 (Kim et al., 2013a, 2013b) with standard parameters to generate the bedGraph files loaded in the IGV browser. For the quantification of m6A methylation, the number of reads per transcript was quantified, both in the meRIP and the cheRNA input, using Salmon (Patro et al., 2017). The methylation level of each transcript was defined as the ratio of the RPKMs in meRIP divided by the RPKMs in the input.

Quantification and Statistical Analysis

Quantification of ChIP-qPCR or RT-qPCR data were carried out with the SDS2.4 software (Applied Biosystems), as specified in the STAR Methods section. Statistical analysis of DNA fibers, immunofluorescence and PLA data were performed with Prism v7 (GraphPad) using the non-parametric Mann-Whitney rank sum test. Statistical comparisons of genomic datasets were done in R (3.6.0 version) using the non-parametric Mann-Whitney rank sum test. Details can be found at the corresponding Figure Legends.

Supplementary Material

Refer to Web version on PubMed Central for supplementary material.

Acknowledgments

We are indebted to Arthur Skoultchi and Encarna Martinez-Salas for reagents and advice, Ana Losada and Ana Cuadrado for help with RNAPII-ChIP, Luciana Gómez-Acuña for help on TT-seq, Sandra Benavente for advice in m6AIP and FTO inhibition, and César Cobaleda for support on computational analysis. We are grateful to the SMOC and Genomic Services at CBMSO and Pepe Belio for art work. We also thank Wendy Bickmore, Andrew Wood, and Andrew Jackson for continuous support during M.G.'s sabbatical stay at the HGU and Ferran Azorin, Jordi Bernues, Victor Corces, Crisanto Gutierrez, and members of M.G. lab for critical reading of the manuscript. Work at the M.G. lab was supported by the Spanish Ministry of Sciences and Innovation (BFU2016-78849-P and PID2019-105949GB-I00, co-financed by the European Union FEDER funds), a CSIC grant (2019AEP004), and a Salvador de Madariaga mobility grant (PRX19/00293). J.M.F.-J., C.S.-M., and J.I.-A. were supported by the Spanish Ministry of Sciences and Innovation fellowships (BES-2014-070050, BES-2017-079897, and PRE2020-095071, respectively); S.M.-V. was supported by a predoctoral fellowship from the Spanish Ministry of Education and Universities (FPU18/04794); and M.S.-P. was supported by an AGAURFI predoctoral fellowship co-financed by Generalitat de Catalunya and the European Social Fund. A.J. was supported by the Spanish Ministry of Sciences and Innovation (BFU2017-82805-C2-1-P and PID2020-112783GB-C21) and J.F.C. by core funding to the MRC Human Genetics Unit from the Medical Research Council (UK).

Data and code availability

- The accession number for the sequencing data reported in this paper is GEO: GSE166426.
- This paper does not report original code.

- Any additional information required to reanalyze the data reported in this paper is available from the lead contact upon request.

References

Abakir A, Giles TC, Cristini A, Foster JM, Dai N, Starczak M, Rubio-Roldan A, Li M, Eleftheriou M, Crutchley J, et al. N6-methyladenosine regulates the stability of RNA:DNA hybrids in human cells. Nat Genet. 2020; 52: 48–55. [PubMed: 31844323]

Almeida R, Fernández-Justel JM, Santa-María C, Cadoret JC, Cano-Aroca L, Lombraña R, Herranz G, Agresti A, Gómez M. Chromatin conformation regulates the coordination between DNA replication and transcription. Nat Commun. 2018; 9 1590 [PubMed: 29686321]

Blinka S, Reimer MH Jr, Pulakanti K, Rao S, Rao S. Superenhancers at the Nanog locus differentially regulate neighboring pluripotency-associated genes. Cell Rep. 2016; 17: 19–28. [PubMed: 27681417]

Cao K, Lailler N, Zhang Y, Kumar A, Uppal K, Liu Z, Lee EK, Wu H, Medrzycki M, Pan C, et al. High-resolution mapping of h1 linker histone variants in embryonic stem cells. PLoS Genet. 2013; 9 e1003417 [PubMed: 23633960]

Cheng Y, Xie W, Pickering BF, Chu KL, Savino AM, Yang X, Luo H, Nguyen DT, Mo S, Barin E, et al. N6-methyladenosine on mRNA facilitates a phase-separated nuclear body that suppresses myeloid leukemic differentiation. Cancer Cell. 2021; 39: 958–972. e8 [PubMed: 34048709]

Ciolfi A, Aref-Eshghi E, Pizzi S, Pedace L, Miele E, Kerkhof J, Flex E, Martinelli S, Radio FC, Ruivenkamp CAL, et al. Frameshift mutations at the C-terminus of HIST1H1E result in a specific DNA hypomethylation signature. Clin Epigenetics. 2020; 12: 7–11. [PubMed: 31910894]

Fan Y, Nikitina T, Zhao J, Fleury TJ, Bhattacharyya R, Bouhassira EE, Stein A, Woodcock CL, Skoultchi AI. Histone H1 depletion in mammals alters global chromatin structure but causes specific changes in gene regulation. Cell. 2005; 123: 1199–1212. [PubMed: 16377562]

Fan Y, Sirotkin A, Russell RG, Ayala J, Skoultchi AI. Individual somatic H1 subtypes are dispensable for mouse development even in mice lacking the H1(0) replacement subtype. Mol Cell Biol. 2001; 21: 7933–7943. [PubMed: 11689686]

Fang H, Clark DJ, Hayes JJ. DNA and nucleosomes direct distinct folding of a linker histone H1 C-terminal domain. Nucleic Acids Res. 2012; 40: 1475–1484. [PubMed: 22021384]

Fyodorov DV, Zhou BR, Skoultchi AI, Bai Y. Emerging roles of linker histones in regulating chromatin structure and function. Nat Rev Mol Cell Biol. 2018; 19: 192–206. [PubMed: 29018282]

García-Muse T, Aguilera A. R Loops: from physiological to pathological roles. Cell. 2019; 179: 604–618. [PubMed: 31607512]

Geeven G, Zhu Y, Kim BJ, Bartholdy BA, Yang SM, Macfarlan TS, Gifford WD, Pfaff SL, Verstegen MJAM, Pinto H, et al. Local compartment changes and regulatory landscape alterations in histone H1-depleted cells. Genome Biol. 2015; 16: 289. [PubMed: 26700097]

Gil N, Ulitsky I. Regulation of gene expression by cis-acting long non-coding RNAs. Nat Rev Genet. 2020; 21: 102–117. [PubMed: 31729473]

Hashimoto H, Takami Y, Sonoda E, Iwasaki T, Iwan H, Tachibana M, Takeda S, Nakayama T, Kimura H, Shinkai Y. Histone H1 null vertebrate cells exhibit altered nucleosome architecture. Nucleic Acids Res. 2010; 38: 3533–3545. [PubMed: 20156997]

Healton SE, Pinto HD, Mishra LN, Hamilton GA, Wheat JC, Swist-Rosowska K, Shukeir N, Dou Y, Steidl U, Jenuwein T, et al. H1 linker histones silence repetitive elements by promoting both histone H3K9 methylation and chromatin compaction. Proc Natl Acad Sci USA. 2020; 117: 14251–14258. [PubMed: 32513732]

Hellauer K, Sirard E, Turcotte B. Decreased expression of specific genes in yeast cells lacking histone H1. J Biol Chem. 2001; 276: 13587–13592. [PubMed: 11278859]

Hergeth SP, Schneider R. The H1 linker histones: multifunctional proteins beyond the nucleosomal core particle. EMBO Rep. 2015; 16: 1439–1453. [PubMed: 26474902]

Europe PMC Funders Author Manuscripts

Izquierdo-Bouldstridge A, Bustillos A, Bonet-Costa C, Aribau-Miralbés P, García-Gomis D, Dabad M, Esteve-Codina A, Pascual-Reguant L, Peiró S, Esteller M, et al. Histone H1 depletion triggers an interferon response in cancer cells via activation of heterochromatic repeats. Nucleic Acids Res. 2017; 45: 11622–11642. [PubMed: 28977426]

Izzo A, Kamieniarz-Gdula K, Ramírez F, Noureen N, Kind J, Manke T, van Steensel B, Schneider R. The genomic landscape of the somatic linker histone subtypes H1.1 to H1.5 in human cells. Cell Rep. 2013; 3: 2142–2154. [PubMed: 23746450]

Jackson DA, Pombo A. Replicon clusters are stable units of chromosome structure: evidence that nuclear organization contributes to the efficient activation and propagation of S phase in human cells. J Cell Biol. 1998; 140: 1285–1295. [PubMed: 9508763]

Juan D, Perner J, Carrillo de Santa Pau E, Marsili S, Ochoa D, Chung HR, Vingron M, Rico D, Valencia A. Epigenomic Co-localization and Co-evolution reveal a key role for 5hmC as a communication hub in the chromatin network of ESCs. Cell Rep. 2016; 14: 1246–1257. [PubMed: 26832418]

Kalashnikova AA, Rogge RA, Hansen JC. Linker histone H1 and protein-protein interactions. Biochim Biophys Acta. 2016; 1859: 455–461. [PubMed: 26455956]

Kalashnikova AA, Winkler DD, McBryant SJ, Henderson RK, Herman JA, Deluca JG, Luger K, Prenni JE, Hansen JC. Linker histone H1.0 interacts with an extensive network of proteins found in the nucleolus. Nucleic Acids Res. 2013; 41: 4026–4035. [PubMed: 23435226]

Khan A, Zhang X. dbSUPER: a database of super-enhancers in mouse and human genome. Nucleic Acids Res. 2016; 44: 164–171. [PubMed: 26384566]

Kim D, Pertea G, Trapnell C, Pimentel H, Kelley R, Salzberg SL. TopHat2: accurate alignment of transcriptomes in the presence of insertions, deletions and gene fusions. Genome Biol. 2013a; 14: R36. [PubMed: 23618408]

Kim JM, Kim K, Punj V, Liang G, Ulmer TS, Lu W, An W. Linker histone H1.2 establishes chromatin compaction and gene silencing through recognition of H3K27me3. Sci Rep. 2015; 5 16714 [PubMed: 26581166]

Kim K, Choi J, Heo K, Kim H, Levens D, Kohno K, Johnson EM, Brock HW, An W. Isolation and characterization of a novel H1.2 complex that acts as a repressor of p53-mediated transcription. J Biol Chem. 2008; 283: 9113–9126. [PubMed: 18258596]

Kim K, Lee B, Kim J, Choi J, Kim JM, Xiong Y, Roeder RG, An W. Linker Histone H1.2 cooperates with Cul4A and PAF1 to drive H4K31 ubiquitylation-mediated transactivation. Cell Rep. 2013b; 5: 1690–1703. [PubMed: 24360965]

Kuleshov MV, Jones MR, Rouillard AD, Fernandez NF, Duan Q, Wang Z, Koplev S, Jenkins SL, Jagodnik KM, Lachmann A, et al. Enrichr: a comprehensive gene set enrichment analysis web server 2016 update. Nucleic Acids Res. 2016; 44: 90–97.

Landau DA, Tausch E, Taylor-Weiner AN, Stewart C, Reiter JG, Bahlo J, Kluth S, Bozic I, Lawrence M, Böttcher S, et al. Mutations driving CLL and their evolution in progression and relapse. Nature. 2015; 526: 525–530. [PubMed: 26466571]

Langmead B, Trapnell C, Pop M, Salzberg SL. Ultrafast and memory-efficient alignment of short DNA sequences to the human genome. Genome Biol. 2009; 10: R25. [PubMed: 19261174]

Lee H, Habas R, Abate-Shen C. MSX1 cooperates with histone H1b for inhibition of transcription and myogenesis. Science. 2004; 304: 1675–1678. [PubMed: 15192231]

Li H, Handsaker B, Wysoker A, Fennell T, Ruan J, Homer N, Marth G, Abecasis G, Durbin R. 1000 Genome project data processing subgroup. the sequence alignment/map (SAM) format and SAMtools. Bioinformatics. 2009; 25: 2078–2079. [PubMed: 19505943]

Li Y, Rivera CM, Ishii H, Jin F, Selvaraj S, Lee AY, Dixon JR, Ren B. CRISPR reveals a distal super-enhancer required for Sox2 expression in mouse embryonic stem cells. PLoS One. 2014; 9 e114485 [PubMed: 25486255]

Liao J, He Y, Szabó PE. The Pou5f1 distal enhancer is sufficient to drive Pou5f1 promoter-EGFP expression in embryonic stem cells. Int J Dev Biol. 2013; 57: 725–729. [PubMed: 24395560]

Liu J, Dou X, Chen C, Chen C, Liu C, Xu MM, Zhao S, Shen B, Gao Y, Han D, He C. N^6-methyladenosine of chromosome-associated regulatory RNA regulates chromatin state and transcription. Science. 2020; 367: 580–586. [PubMed: 31949099]

Liu J, Gao M, He J, Wu K, Lin S, Jin L, Chen Y, Liu H, Shi J, Wang X, et al. The RNA m6A reader YTHDC1 silences retrotransposons and guards ES cell identity. Nature. 2021; 591: 322–326. [PubMed: 33658714]

Love MI, Huber W, Anders S. Moderated estimation of fold change and dispersion for RNA-seq data with DESeq2. Genome Biol. 2014; 15: 550. [PubMed: 25516281]

Lu X, Hansen JC. Identification of specific functional subdomains within the linker histone H10 C-terminal domain. J Biol Chem. 2004; 279: 8701–8707. [PubMed: 14668337]

Maslon MM, Braunschweig U, Aitken S, Mann AR, Kilanowski F, Hunter CJ, Blencowe BJ, Kornblihtt AR, Adams IR, Cáceres JF. A slow transcription rate causes embryonic lethality and perturbs kinetic coupling of neuronal genes. EMBO J. 2019; 38 e101244 [PubMed: 30988016]

Meyer KD, Saletore Y, Zumbo P, Elemento O, Mason CE, Jaffrey SR. Comprehensive analysis of mRNA methylation reveals enrichment in 3' UTRs and near stop codons. Cell. 2012; 149: 1635–1646. [PubMed: 22608085]

Mi H, Muruganujan A, Huang X, Ebert D, Mills C, Guo X, Thomas PD. Protocol Update for large-scale genome and gene function analysis with the PANTHER classification system (v.14.0). Nat Protoc. 2019; 14: 703–721. [PubMed: 30804569]

Millán-Ariño L, Islam ABMMK, Izquierdo-Bouldstridge A, Mayor R, Terme JM, Luque N, Sancho M, López-Bigas N, Jordan A. Mapping of six somatic linker histone H1 variants in human breast cancer cells uncovers specific features of H1.2. Nucleic Acids Res. 2014; 42: 4474–4493. [PubMed: 24476918]

Nesterova TB, Wei G, Coker H, Pintacuda G, Bowness JS, Zhang T, Almeida M, Bloechl B, Moindrot B, Carter EJ, et al. Systematic allelic analysis defines the interplay of key pathways in X chromosome inactivation. Nat Commun. 2019; 10 3129 [PubMed: 31311937]

Patil DP, Chen CK, Pickering BF, Chow A, Jackson C, Guttman M, Jaffrey SR. m6A RNA methylation promotes XIST-mediated transcriptional repression. Nature. 2016; 537: 369–373. [PubMed: 27602518]

Patro R, Duggal G, Love MI, Irizarry RA, Kingsford C. Salmon provides fast and bias-aware quantification of transcript expression. Nat Methods. 2017; 14: 417–419. [PubMed: 28263959]

Porman AM, Roberts JT, Dunca ED, Chrupcala ML, Levine AA, Kennedy MA, Williams MM, Richer JK, Johnson AM. A single N6-methyladenosine site in lncRNA HOTAIR regulates its function in breast cancer cells. Preprint at bioRxiv. 2020; doi: 10.1101/2020.06.08.14095

Reddy A, Zhang J, Davis NS, Moffitt AB, Love CL, Waldrop A, Leppa S, Pasanen A, Meriranta L, Karjalainen-Lindsberg ML, et al. Genetic and functional drivers of diffuse large B cell lymphoma. Cell. 2017; 171: 481–494. e15 [PubMed: 28985567]

Ries RJ, Zaccara S, Klein P, Olarerin-George A, Namkoong S, Pickering BF, Patil DP, Kwak H, Lee JH, Jaffrey SR. M6A enhancesthe phase separation potential of mRNA. Nature. 2019; 571: 424–428. [PubMed: 31292544]

Roque A, Iloro I, Ponte I, Arrondo JLR, Suau P. DNA-induced secondary structure of the carboxyl-terminal domain of histone H1. J Biol Chem. 2005; 280: 32141–32147. [PubMed: 16006555]

Roundtree IA, Luo GZ, Zhang Z, Wang X, Zhou T, Cui Y, Sha J, Huang X, Guerrero L, Xie P, et al. YTHDC1 mediates nuclear export of N-6-methyladenosine methylated mRNAs. Elife. 2017; 6 e31311 [PubMed: 28984244]

Saitoh N, Spahr CS, Patterson SD, Bubulya P, Neuwald AF, Spector DL. Proteomic analysis of interchromatin granule clusters. Mol Biol Cell. 2004; 15: 3876–3890. [PubMed: 15169873]

Sancho M, Diani E, Beato M, Jordan A. Depletion of human histone H1 variants uncovers specific roles in gene expression and cell growth. PLoS Genet. 2008; 4 e1000227 [PubMed: 18927631]

Schwalb B, Michel M, Zacher B, Frühauf K, Demel C, Tresch A, Gagneur J, Cramer P. TT-seq maps the human transient transcriptome. Science. 2016; 352: 1225–1228. [PubMed: 27257258]

Serna-Pujol N, Salinas-Pena M, Mugianesi F, Lopez-Anguita N, Torrent-Llagostera F, Izquierdo-Bouldstridge A, Marti-Renom MA, Jordan A. TADs enriched in histone H1.2 strongly overlap with the B compartment, inaccessible chromatin, and AT-rich Giemsa bands. FEBS J. 2020; 288: 1989–2013. [PubMed: 32896099]

Shen X, Gorovsky MA. Linker histone H1 regulates specific gene expression but not global transcription in vivo. Cell. 1996; 86: 475–483. [PubMed: 8756729]

Szerlong HJ, Herman JA, Krause CM, DeLuca JG, Skoultchi A, Winger QA, Prenni JE, Hansen JC. Proteomic characterization of the nucleolar linker histone H1 interaction network. J Mol Biol. 2015; 427: 2056–2071. [PubMed: 25584861]

Trapnell C, Williams BA, Pertea G, Mortazavi A, Kwan G, van Baren MJ, Salzberg SL, Wold BJ, Pachter L. Transcript assembly and quantification by RNA-Seq reveals unannotated transcripts and isoform switching during cell differentiation. Nat Biotechnol. 2010; 28: 511–515. [PubMed: 20436464]

Vujatovic O, Zaragoza K, Vaquero A, Reina O, Bernués J, Azorín F. *Drosophila melanogaster* linker histone dH1 is required for transposon silencing and to preserve genome integrity. Nucleic Acids Res. 2012; 40: 5402–5414. [PubMed: 22406835]

Wei G, Almeida M, Pintacuda G, Coker H, Bowness JS, Ule J, Brockdorff N. Acute depletion of METTL3 implicates N6-methyladenosine in alternative intron/exon inclusion in the nascent transcriptome. Genome Res. 2021; 31: 1395–1408. [PubMed: 34131006]

Werner MS, Ruthenburg AJ. Nuclear fractionation reveals thousands of chromatin-tethered noncoding RNAs adjacent to active genes. Cell Rep. 2015; 12: 1089–1098. [PubMed: 26257179]

Werner MS, Sullivan MA, Shah RN, Nadadur RD, Grzybowski AT, Galat V, Moskowitz IP, Ruthenburg AJ. Chromatin-enriched lncRNAs can act as cell-type specific activators of proximal gene transcription. Nat Struct Mol Biol. 2017; 24: 596–603. [PubMed: 28628087]

Willcockson MA, Healton SE, Weiss CN, Bartholdy BA, Botbol Y, Mishra LN, Sidhwani DS, Wilson TJ, Pinto HB, Maron MI, et al. H1 histones control the epigenetic landscape by local chromatin compaction. Nature. 2021; 589: 293–298. [PubMed: 33299182]

Wolffe AP. Histone H1. Int J Biochem Cell Biol. 1997; 29: 1463–1466. [PubMed: 9570139]

Woodcock CL, Skoultchi AI, Fan Y. Role of linker histone in chromatin structure and function: H1 stoichiometry and nucleosome repeat length. Chromosome Res. 2006; 14: 17–25. [PubMed: 16506093]

Xiao W, Adhikari S, Dahal U, Chen YS, Hao YJ, Sun BF, Sun HY, Li A, Ping XL, Lai WY, et al. Nuclear m(6)A reader YTHDC1 regulates mRNA splicing. Mol Cell. 2016; 61: 507–519. [PubMed: 26876937]

Xu W, Li J, He C, Wen J, Ma H, Rong B, Diao J, Wang L, Wang J, Wu F, et al. METTL3 regulates heterochromatin in mouse embryonic stem cells. Nature. 2021; 591: 317–321. [PubMed: 33505026]

Yan Q, Shields EJ, Bonasio R, Sarma K. Mapping native R-lops genome-wide using a targeted nuclease approach. Cell Rep. 2019; 29: 1369–1380. e5 [PubMed: 31665646]

Yusufova N, Kloetgen A, Teater M, Osunsade A, Camarillo JM, Chin CR, Doane AS, Venters BJ, Portillo-Ledesma S, Conway J, et al. Histone H1 loss drives lymphoma by disrupting 3D chromatin architecture. Nature. 2021; 589: 299–305. [PubMed: 33299181]

Zaccara S, Ries RJ, Jaffrey SR. Reading, writing and erasing mRNA methylation. Nat Rev Mol Cell Biol. 2019; 20: 608–624. [PubMed: 31520073]

Zeng Y, Wang S, Gao S, Soares F, Ahmed M, Guo H, Wang M, Hua JT, Guan J, Moran MF, et al. Refined RIP-seq protocol for epitran-scriptome analysis with low input materials. PLoS Biol. 2018; 16 e2006092 [PubMed: 30212448]

Zhang P, Branson OE, Freitas MA, Parthun MR. Identification of replication-dependent and replication-independent linker histone complexes: tpr specifically promotes replication-dependent linker histone stability. BMC Biochem. 2016; 17: 18. [PubMed: 27716023]

Zhang Y, Cooke M, Panjwani S, Cao K, Krauth B, Ho PY, Medrzycki M, Berhe DT, Pan C, McDevitt TC, Fan Y. Histone H1 depletion impairs embryonic stem cell differentiation. PLoS Genet. 2012; 8 e1002691 [PubMed: 22589736]

Zhang Y, Liu T, Meyer CA, Eeckhoute J, Johnson DS, Bernstein BE, Nusbaum C, Myers RM, Brown M, Li W, Liu XS. Modelbased analysis of ChIP-seq (MACS). Genome Biol. 2008; 9 R137 [PubMed: 18798982]

Europe PMC Funders Author Manuscripts

Highlights

- Reducing histone H1 content unveils thousands of chromatin-bound regulatory ncRNAs
- Upon H1 depletion, ncRNAs are actively transcribed and have reduced levels of m6A
- Low m6A levels at ncRNAs cause conflicts with incoming DNA replication forks
- Impairing m6A pathway rescues replication-transcription conflicts at H1-depleted cells

Europe PMC Funders Author Manuscripts

In brief

Fernández-Justel et al. report an unexpected role for histone H1 in the regulation of non-coding RNA production and turnover with important implications for genome maintenance. They uncover a link between chromatin conformation imparted by histone H1 and the m6A gene-regulatory axis.

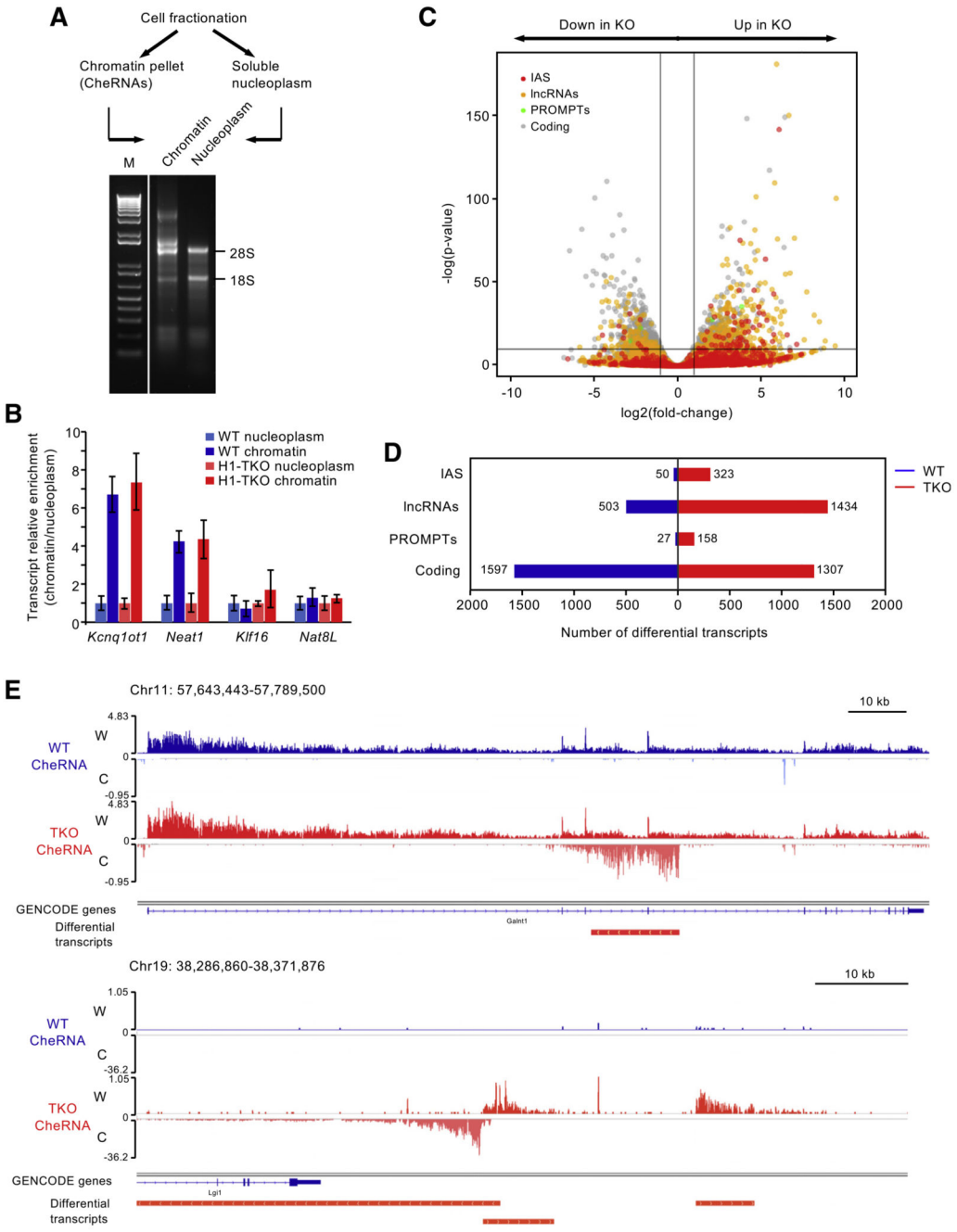

Figure 1. Histone H1-deficient cells specifically accumulate non-coding transcripts on chromatin

(A) Schematics of CheRNA purification and representative example of chromatin and nucleoplasmic RNA fractions run in a non-denaturing 1% agarose gel. M, 1 kb ladder. (B) Ratio between chromatin and nucleoplasmic levels for the indicated RNAs: *Kncqlotl* and *Neat1* lncRNAs associate to chromatin post-transcriptionally (Werner and Ruthenburg, 2015), whereas *Klf16* and *Nat8L* mRNAs do not. Quantitative real-time PCR data represent the mean and SD of three biological replicates of WT and H1-TKO mES cell preparations. Blue, WT cells; red, H1-TKO cells. Primer sequences are listed in Table S1.

Europe PMC Funders Author Manuscripts

(C) Volcano plot showing the $\log_2$(fold change) and the –log(p value) for the indicated CheRNA classes between WT and H1-TKO cells: internal antisense (IAS), lncRNAs, promoter upstream transcripts (PROMPTs), and coding RNAs. See Figure S1 fortranscript classification.
(D) Number of differentially expressed transcripts between WT and H1-TKO cells for each CheRNA category. Blue, overexpressed in WT; red, over-expressed in H1-TKO cells.
(E) Representative IGV browser snapshots of transcripts specifically accumulated in the chromatin of H1-TKO cells. Upper panel: IAS for the *Galnt10* gene. Lower panel: several lncRNAs adjacent to the silent *Lgi1* gene.

Europe PMC Funders Author Manuscripts

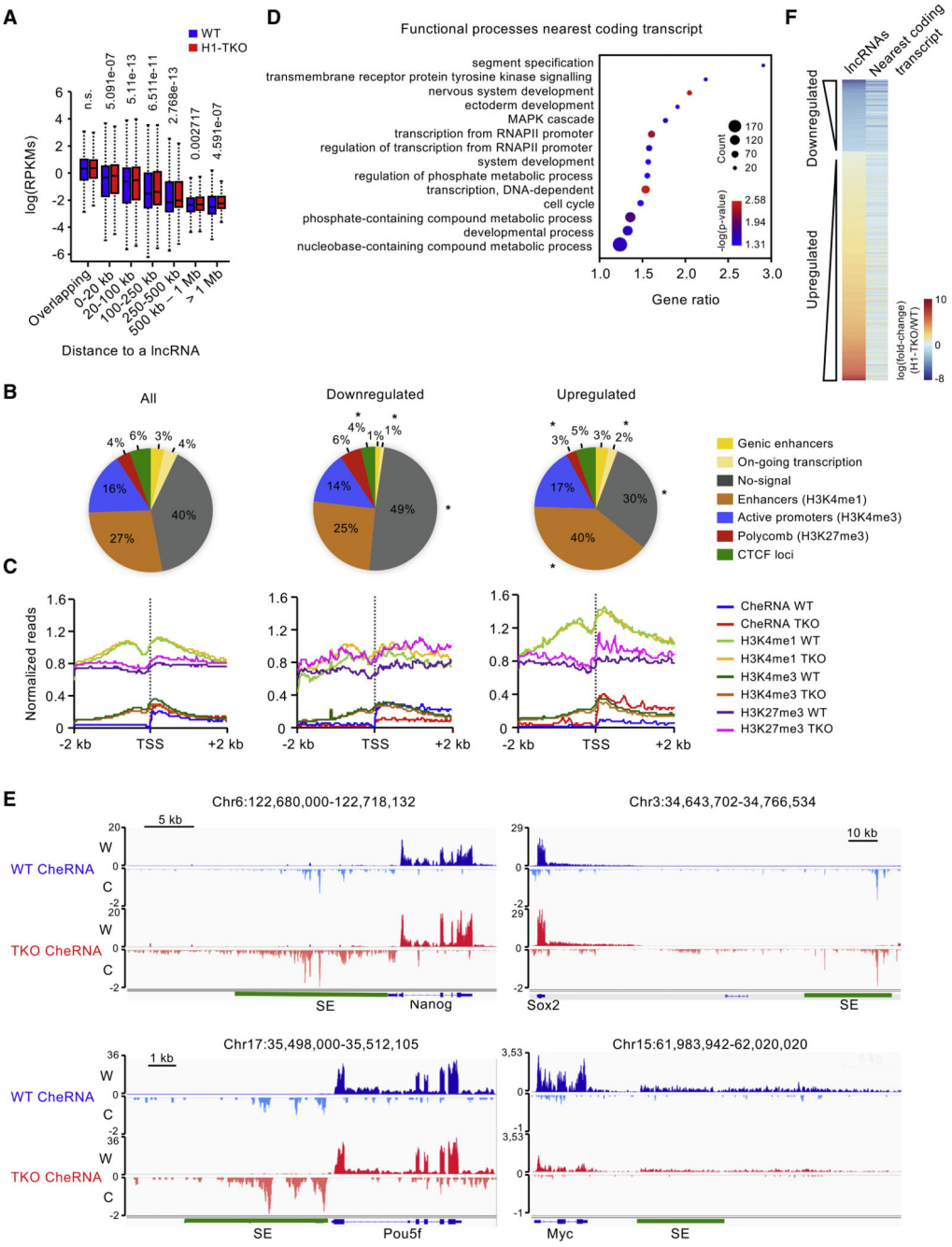

Figure 2. Accumulated non-coding transcripts are cis-regulatory RNAs

(A) Distribution of log(RPKMs) of coding genes located at the distances shown of a lncRNA. Blue, WT cells; red, H1-TKO cells. Statistical differences between cell types are noted above (Mann-Whitney test).

(B) Percentage of lncRNAs whose TSS matches each of the chromatin states shown. The percentage was compared with the expected one obtained from 100 random permutations of the differential transcripts, and the p value was calculated. *p < 0.01. Chromatin states are from Juan et al. (2016).

Europe PMC Funders Author Manuscripts

(C) Profile of CheRNA-seq and ChIP-seq signal of the indicated histone marks plotted in 4 kb windows surrounding the TSS of the lncRNA's categories is shown. H3K4me1 WT and TKO signals were multiplied by a scale factor of 2 to facilitate visualization in a single plot. ChIP-seq data are from Geeven et al.(2015).

(D) Gene Ontology (GO)-term enrichment analysis of the set of genes proximal to a differential lncRNA. The observed/expected ratio is represented in the X axis. The size and color of the dots match the number of enriched genes and the adjusted p value, respectively.

(E) IGV browser snapshots of lncRNAs derived from the annotated enhancers regulating *Nanog* and *Sox2* (upper panel) and *Pou5f* (*Oct4*) and *Myc* genes (lower panel). Note that in the case of *Myc*, there is a parallel downregulation of the gene and the lncRNA derived from the SE in H1-TKO cells, while for the other three examples there is an upregulation of the SE-derived lncRNAs with no change in the expression levels of their corresponding coding genes.

(F) Heatmap showing the expression fold changes of upregulated or downregulated lncRNAs and the neighboring coding gene. See also Figure S2.

Europe PMC Funders Author Manuscripts

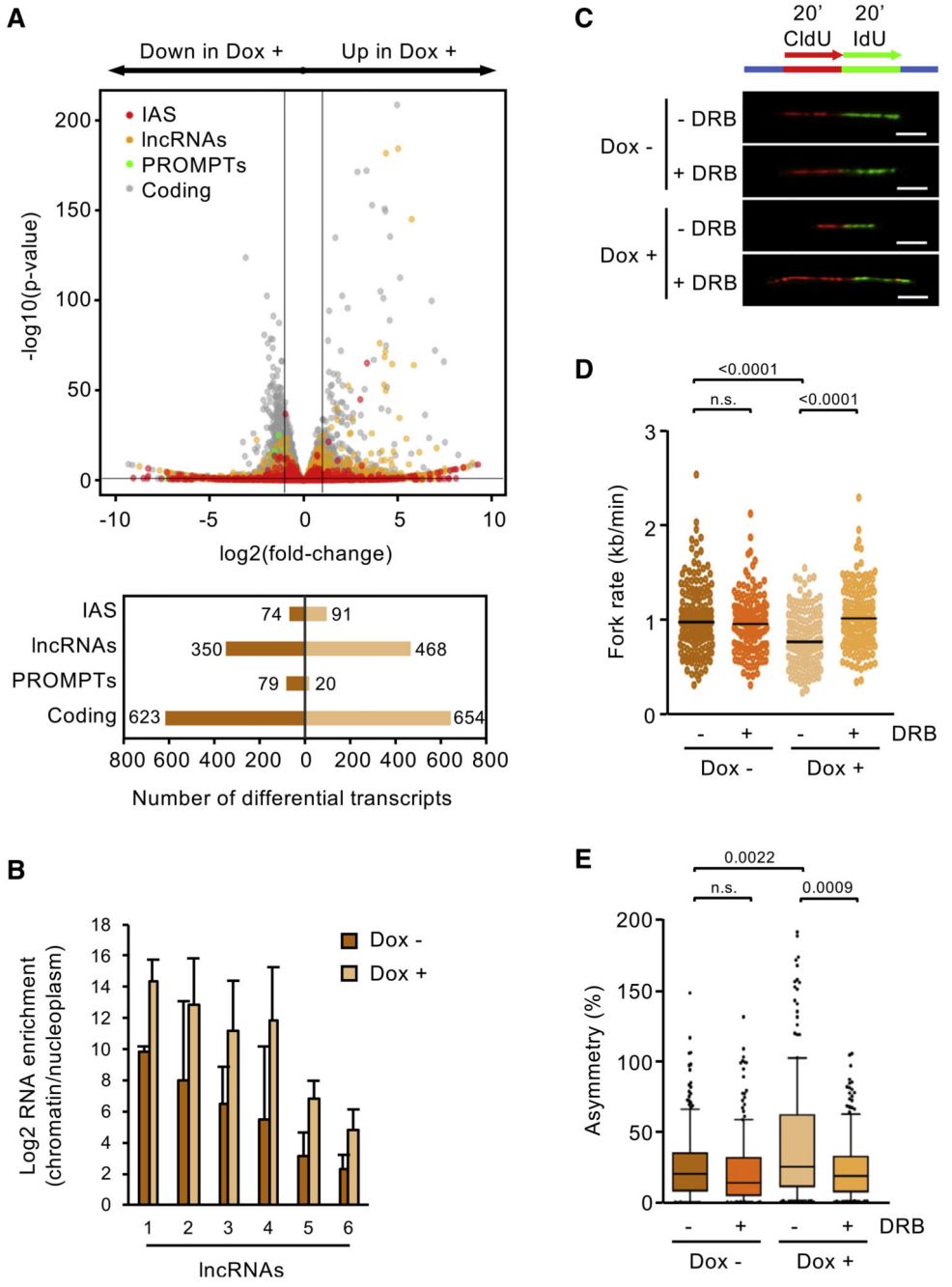

Figure 3. lncRNA overexpression and transcription-dependent replicative stress upon inducible knockdown of histone H1 in human cells

(A) Volcano plot showing the $\log_2$(fold change) and the –log(p value) for each transcript in shMultiH1 T47D Dox+ cells relative to Dox– cells. The number of differential expressed transcripts for each category is shown below. Total RNA-seq data are from Izquierdo-Boulstridge et al. (2017).

(B) Chromatin/nucleoplasm enrichment of 6 lncRNAs in T47D shMultiH1 ± Dox. Quantitative real-time PCR data represent mean and SD of four independent RNA

preparations, expressed as ratio relative to nucleoplasm (Dox–) (n = 4). Primer sequences are listed in Table S2.

(C) Representative example of DNA fibers from Dox– and Dox+ shMultiH1 cells labeled sequentially for 20 min with CldU (red) and IdU (green) in conditions of active (−DRB) or blocked (+DRB) transcription elongation used to estimate fork rates and fork asymmetries. Scale bar, 5 μm.

(D and E) Measure of DNA replication fork rate (D), and fork asymmetry (E), in Dox– and Dox+ shMultiH1 cells untreated (−DRB) or treated for 3 h with DRB (+DRB). Median values are indicated. Data shown are pooled from two independent experiments. Statistical differences between distributions were assessed with the Mann-Whitney rank-sum test.

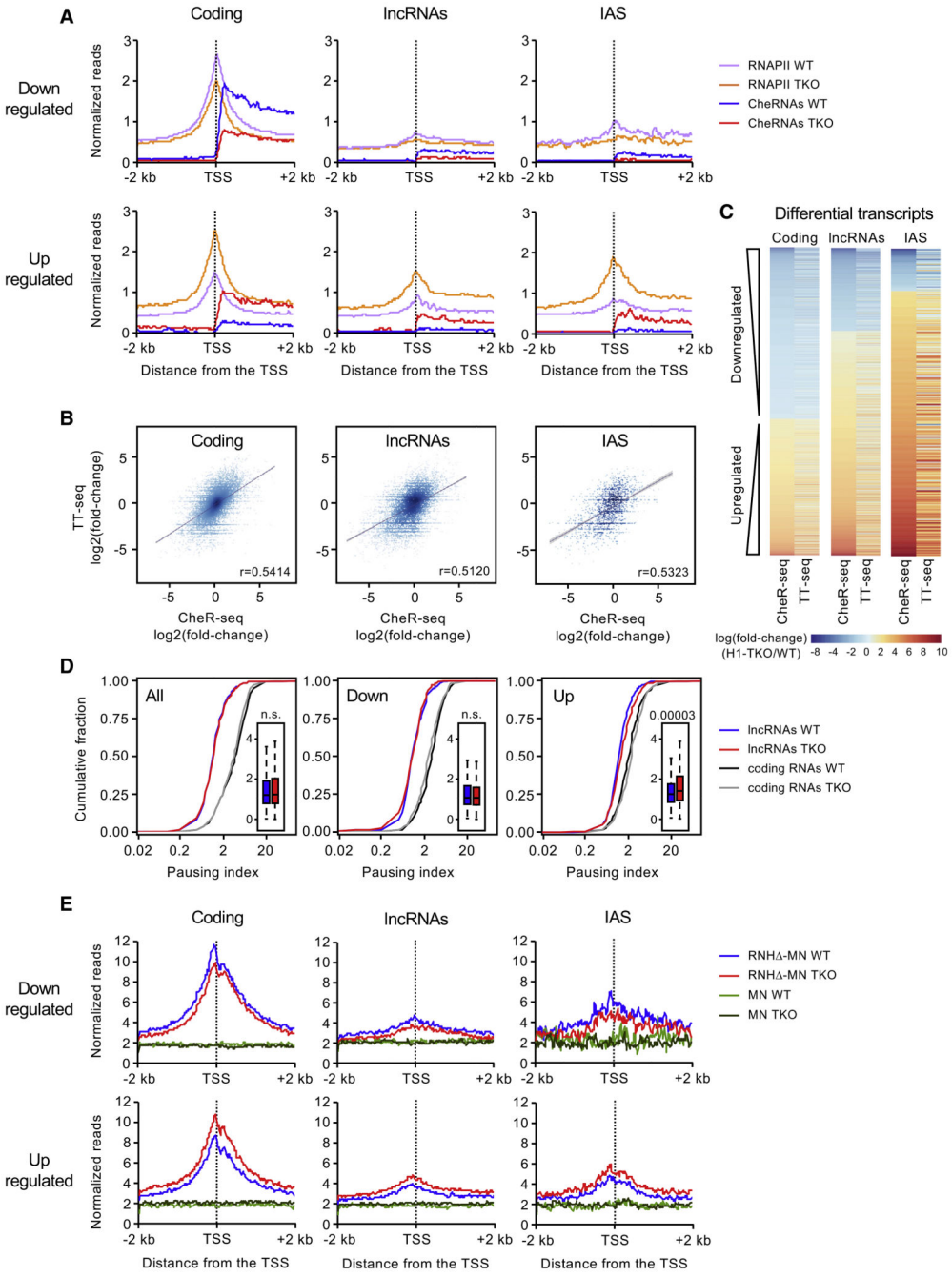

Figure 4. Accumulated transcripts are transcribed at high rates and tethered to chromatin by RNAPII

(A) Metaplots of RNAPII-seq and CheRNA-seq spike-in normalized signals at the indicated transcript categories in WT and H1-TKO cells, plotted in a 4kb window around the TSS. Note that the TSS position at IAS refers to the antisense strand of the coding gene. RNAPII WT and TKO signals were multiplied by a scale factor of 1:2, to facilitate visualization in a single plot. See Figures S4A–S4F for further details on RNAPII ChIP-seq data.

(B) Relationship between chromatin abundance fold changes (CheR-seq) and transcriptional rate fold changes (TT-seq) at the indicated transcript categories. See also Figure S4G.

Europe PMC Funders Author Manuscripts

(C) Heatmap representation of CheRNA-seq and TT-seq fold changes between H1-TKO/WT conditions at differential transcripts.
(D) Cumulative distribution and boxplots (inside) of RNAPII pausing index at the indicated transcript categories in WT and H1-TKO cells. p values were calculated by a Mann-Whitney U test.
(E) Metaplots of MapR normalized signal at the indicated transcript categories in WT and H1-TKO cells, plotted in a 4 kb window around the TSS. See Figure S5 for details of R-loop abundance determination by MapR.

Europe PMC Funders Author Manuscripts

Europe PMC Funders Author Manuscripts

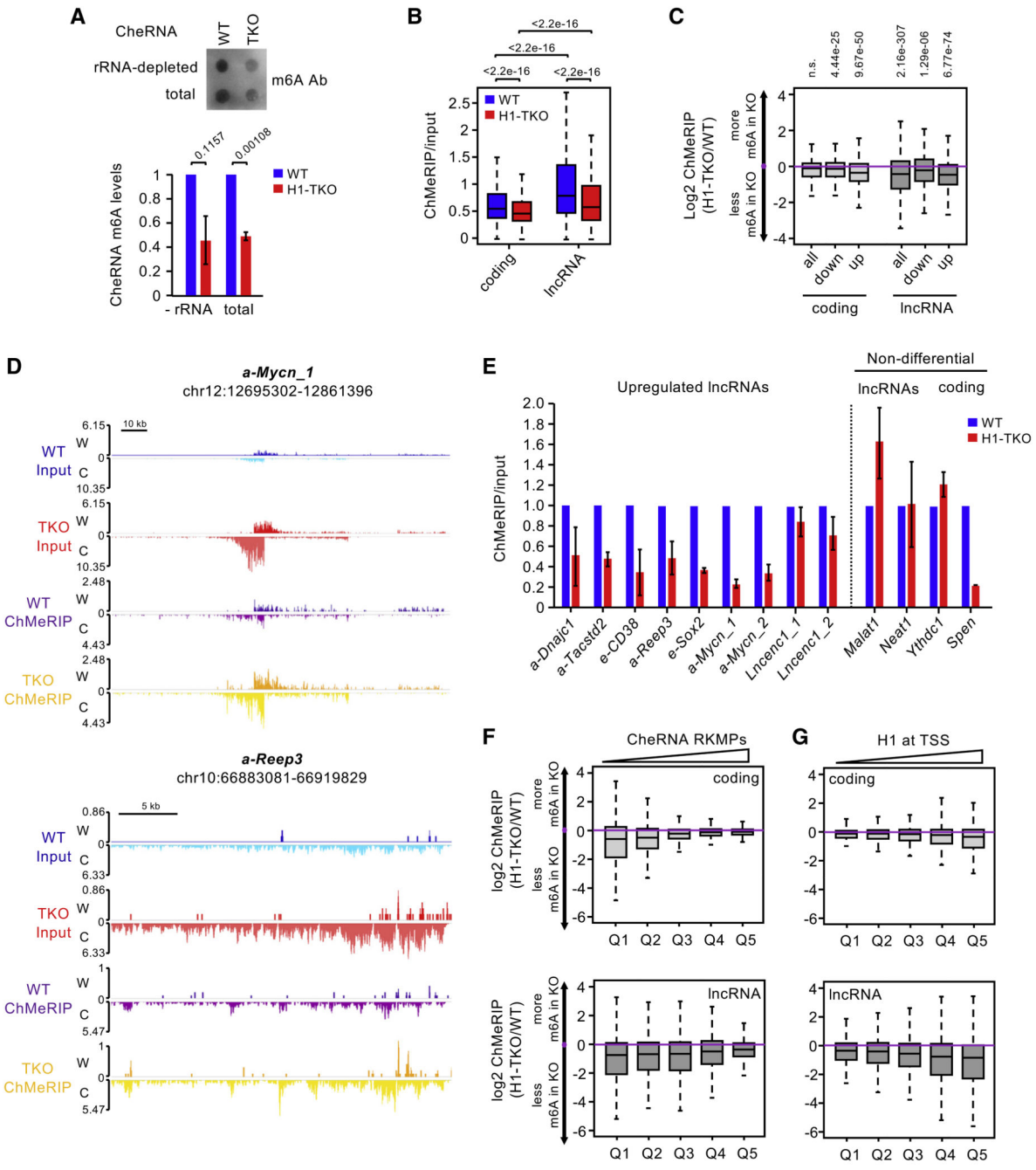

Figure 5. Accumulated lncRNAs in H1-TKO cells have reduced levels of m6A modification

(A) Dot-blot quantification of m6A levels on 300 ng rRNA-depleted or 5 μg total CheRNA preparations from WT and H1-TKO cells. n = 3 biological replicates, error bars indicate means ± SD. p values are shown (one-sample t test).

(B) ChMeRIP RPKMs for coding and non-coding transcripts, normalized by the RPKMs in the CheRNA input. p values are shown on top (Mann-Whitney U test). See also Figure S6.

(C) Plots showing the ratios of normalized ChMeRIP read counts relative to input between H1-TKO and WT cells (log_2H1-TKO/WT) at the indicated transcript categories. p values for the comparisons are shown on top (one-sample Wilcoxon rank-sum test).
(D) Representative IGV screenshots showing normalized reads from ChMeRIP-seq and the corresponding CheRNA-seq inputs of two differentially abundant lncRNAs in WT and H1-TKO cells.
(E) m6A levels of 9 upregulated lncRNAs quantified through normalizing ChMeRIP qPCR results with spike-in between WT and H1-TKO cells. Data from two non-differential coding and lncRNAs with defined m6A peaks are also shown on the right. The IGV tracks of ChMeRIP reads of these m6A-modified transcripts are shown in Figures S6B and S6C. n = 2 biological replicates; error bars indicate means ± SD. Upregulated lncRNAs are named relative to the location to the nearest coding gene. Primer sequences are listed in Table S1.
(F) ChMeRIP ratios between H1-TKO and WT cells across 5 quantiles of increasing chromatin transcript levels for coding (upper plot) or lncRNA (lower plot). CheRNA RKPMs are from WT cells.
(G) Same as in (F) across 5 quantiles of increasing histone H1 levels at ±2 kb of the TSS. H1 ChIPseq data in WT cells are from Cao et al. (2013). In all cases boxplots denote the medians and the interquantile ranges, and the whiskers represent the 10th and 90th percentiles.

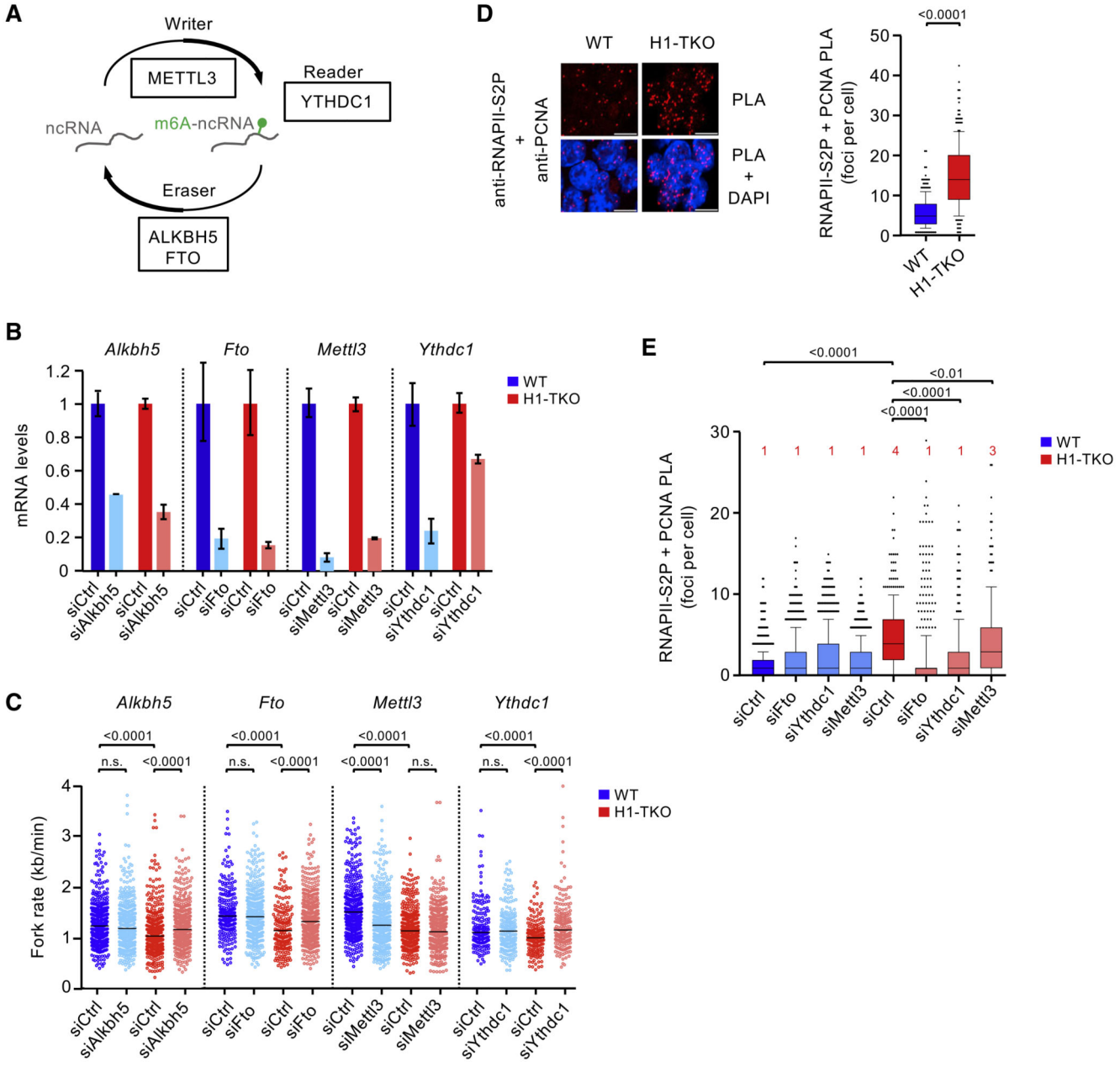

Figure 6. Impairing m6A demethylase activity in H1-TKO cells decreases lncRNA abundance on chromatin and rescues the speed of replication forks

(A) Simplified scheme ofthe m6A modification pathway.

(B) Quantitative real-time PCR mRNA silencing levels of *Alkbh5*, *Fto*, *Mettl3*, and *Ythdcl* 24 h after cellular transfection with the indicated specific siRNAs. mRNA levels were normalized to *Hprt* mRNA levels at each condition. Data showthe median ± SD of two independent replicates (n = 2). Primer sequences are listed in Table S1 and siRNA sequences in Table S3.

(C) Replication fork rates of WT and H1-TKO cells transfected with the indicated siRNAs. Median values are indicated. Data shown are pooled from two independent experiments (n

> 410). Statistical differences between distributions were assessed with the Mann-Whitney rank-sum test. See also Figure S7.

(D) Representative RNAPII-S2P + PCNA PLA images and quantification of PLA foci per cell in WT and H1-TKO cells. PLA foci are represented as boxplots(n = 2), where the center line indicates the median and the boxes and whiskers indicate 25th to 75th and 10th to 90th percentiles, respectively. Foci numbers per cell below and above the whiskers are drawn as individual points (Mann-Whitney U test). Scale bar, 10 μM. PLA controls are shown in Figure S7F.

(E) Same as in (D) in cells transfected with the indicated siRNAs (n = 2). Median values are indicated. More than 300 cells/condition were quantified.

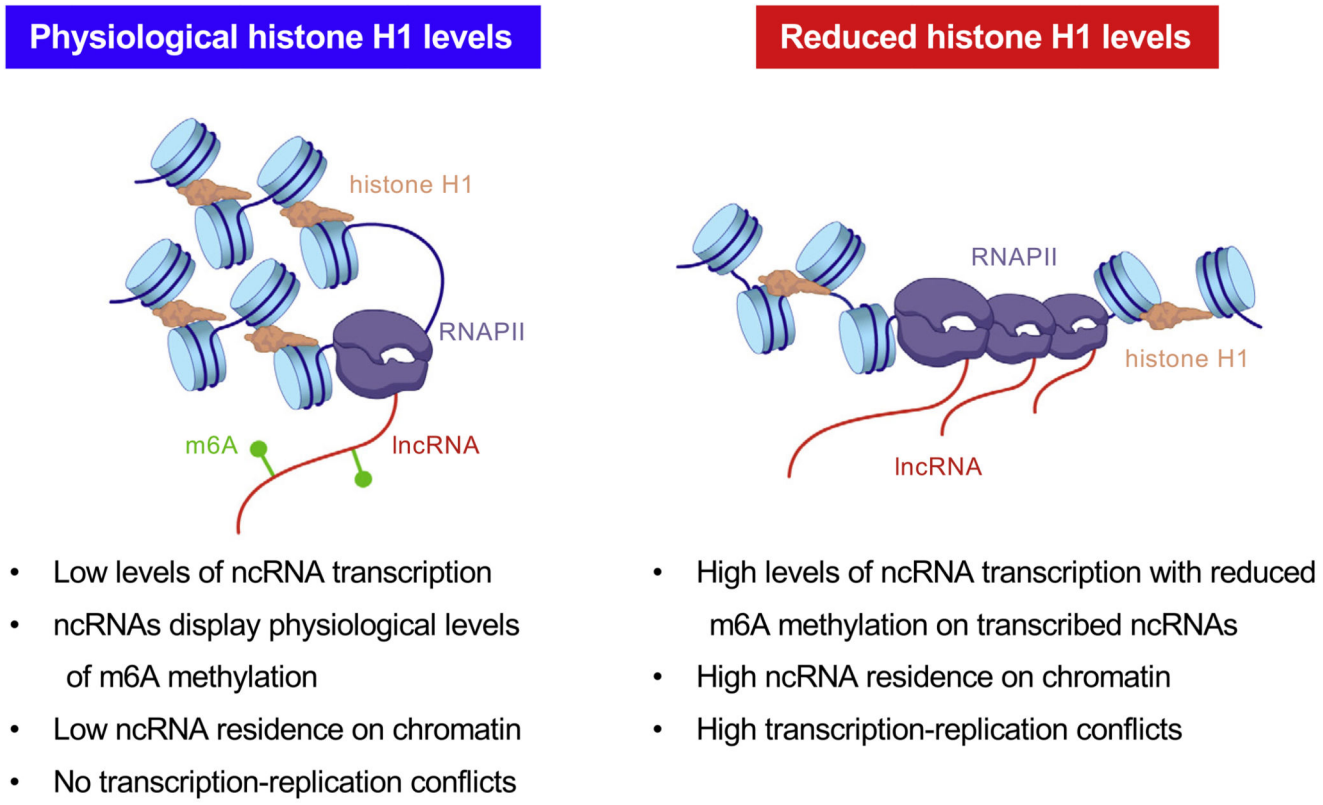

Figure 7. Cartoon representing the impact of histone H1 levels on ncRNA turnover on chromatin

Under physiological H1 levels, transcription of ncRNAs is reduced and those ncRNAs that remain present display high levels of m6A methylation. Upon H1 depletion, there is an increased recruitment of RNAPII complexes driving transcription of ncRNAs. These nascent ncRNAs, in addition, have reduced levels of m6A modification, which causes their stabilization on chromatin, generating conflicts with incoming DNA replication forks.